THESIS

# DEVELOPMENT OF A PLUME IDENTIFICATION ALGORITHM FOR OPTICAL GAS IMAGING OF NATURAL GAS EMISSIONS THAT REQUIRES NO HUMAN INTERVENTION

Submitted by

Marcus M. Martinez

Department of Mechanical Engineering

In partial fulfillment of the requirements

For the Degree of Master of Science

Colorado State University

Fort Collins, Colorado

Spring 2020

Master's Committee:

Advisor: Anthony Marchese
Co-Advisor: Daniel Zimmerle

Joe von Fischer

ABSTRACT

DEVELOPMENT OF A PLUME IDENTIFICATION ALGORITHM FOR OPTICAL GAS IMAGING OF NATURAL GAS EMISSIONS THAT REQUIRES NO HUMAN INTERVENTION

Recent growth in natural gas production in the United States has increased focus on reducing greenhouse gas emissions from the natural gas supply chain. Methane, the primary constituent of natural gas, is also a potent greenhouse gas. Optical gas imaging (OGI) is frequently used for emission detection in upstream and midstream sectors of the natural gas supply chain. Current OGI methods typically use mid-range infrared video cameras tuned to absorption lines of light hydrocarbons to make natural gas emissions visible to human operators. Prior studies of camera output have used human interpretation to determine if an emission is visible in the video stream, making it difficult to standardize measures of visibility between tests or to automate large test suites. This work presents a signal processing method which separates the background scene from the gas plume when used in controlled test conditions where video is collected in both leaking and non-leaking conditions. The method utilizes a novel frequency-based method that detects the high-frequency motion of the gas plume in the video stream. After background removal, the size of the gas plume can be quantified by thresholding the detected plume and measuring its size relative to the camera's field of view. The resulting metric eliminates the need for human evaluation of video streams. To demonstrate application of the method, multiple cameras were used to develop a relationship between emission rate and plume visibility over a range of viewing distances. Tests were conducted at the *Methane Emissions Technology Evaluation Center*, on CSU's Foothills Campus, using six identical OGI cameras (FLIR G300a camera cores with 38 mm lenses) to image the emission from multiple directions at a range 1 to 6 m. Gas was released from a mock well head at 17 to 196 g/h, with wind speeds of 1.8 to 3.0 m/s. Comparison with expert

evaluation was used to set and validate the threshold levels; a 90% probability of detection requires a plume covering at least 13.8% of the camera's field of view. Testing indicated a linear relationship between emission rate and plume coverage fractions at a distance of 1 to 2 m, regardless of the viewing angle. Beyond 2 m, plume coverage drops rapidly, approaching the noise floor. While test conditions were limited, sufficient data was collected to demonstrate method functionality and its applicability to evaluating OGI emission detection systems.

## ACKNOWLEDGEMENTS

First, I must thank Dan Zimmerle for the opportunity to pursue natural gas research at Colorado State University. I am sure, without Dan's support, there is no chance I could have completed any work that could be used towards a thesis. Without his immense patience, knowledge, and devotion I do not think I would be where I am today, and for that I must express my utmost gratitude.

On that note, Anthony Marchese devoted many hours of time in joining weekly meetings to provide needed support and comic relief through challenging times and confusion when iterating to create a functional algorithm for this work. Without him giving me the opportunity to interview for an undergraduate position at METEC, I am sure I would not have completed this work in just two years.

Countless others deserve thanks for their support in this work. Interviewing with Clay my first semester junior year to work to maintain METEC and provide some undergraduate research support was the primary reason I even entered the natural gas field. Furthermore, he then invested countless hours in me to help me get this project off the ground. Without his support, I am confident I would still be trying to understand how to control six cameras simultaneously. Aidan, thank you for the constant support during the sometimes grueling experiment days and fielding my constant calls of questions when running the experiments. Becky and Ian provided a great help to get this project off the ground and moving. Becky acted as someone to talk to when things seemed far too overwhelming and confusing. Ian performed the absolutely necessary role in the development of the camera control program and export tool. Without his knowledge, I am confident I would still be trying to learn C#.

Mostly important, my family. I am eternally grateful to my parents in providing me an excellent childhood to grow and pursue my interests. My Dad, the chemical engineer, definitely gave me his work ethic, engineering mindset, and fueled my excitement in pursuing engineering since I was a kid. My Mom, the third grade teacher, taught me how to follow through then achieve my goals, and showed me the love, care, and support I needed when things got tough. My older siblings, Matt

and Nicole, showed me how to relax and have a good time every once in awhile. The random *Fam Crew Party 3.0* messages never failed in making me smile. Thank you to my Grandparents, in-state and out-of-state. Namely, Grandma and Grandpa Roegiers, Grandma and Grandpa Martinez, and Martie and Les from across the cul de sac. You all are part of the reason I am who I am today.

Finally, my AV Engineering hall mates freshman year that have now transformed into my best friends. The countless dorm, Rams Village, then Casa Blanca shenanigans we experienced are things that I will always cherish. I am forever grateful I met you all. These are truly the good old days.

If for whatever reason you find yourself reading this, its too late to stop now! See you at the end.

# DEDICATION

*To my Family:*

*Jim, Dawn, Matt, and Nicole Martinez*

*"The true meaning of life is to plant trees, under whose shade you do not expect to sit."*

*And Scotty Boo Boo, of course*

TABLE OF CONTENTS


| | | |
|---|---|---|
| ABSTRACT | | ii |
| ACKNOWLEDGEMENTS | | iv |
| DEDICATION | | vi |
| LIST OF TABLES | | ix |
| LIST OF FIGURES | | x |
| Chapter 1 | Introduction | 1 |
| 1.1 | Motivation | 1 |
| 1.2 | Optical Gas Imaging Background | 2 |
| 1.3 | Related Computational OGI Detection Work | 3 |
| 1.3.1 | Smoke Detection | 3 |
| 1.3.2 | OGI Deep Learning | 4 |
| 1.3.3 | Commercial Products | 5 |
| 1.3.4 | Predictive Models | 6 |
| 1.4 | Objective and Overview | 7 |
| Chapter 2 | OGI Fundamentals | 9 |
| 2.1 | Infrared Fundamentals and Imaging Properties | 9 |
| 2.1.1 | Infrared Fundamentals | 9 |
| 2.1.2 | Imaging Properties | 10 |
| 2.2 | Description of Data Acquisition | 12 |
| 2.2.1 | Development of Imaging Software | 13 |
| 2.2.2 | Data Processing Pipeline | 14 |
| Chapter 3 | Gas Temperature Differential and Camera Background Experiment | 16 |
| 3.1 | Background Motivation | 16 |
| 3.2 | Gas Temperature Differential Design of Experiment | 17 |
| 3.3 | Gas Temperature Differential Experimental Setup | 19 |
| 3.3.1 | Camera Imaging Background Control | 19 |
| 3.3.2 | Plume Temperature Control Unit | 20 |
| 3.3.3 | Camera Wiring Configuration | 22 |
| 3.4 | Inconclusive Quantitative Results | 22 |
| 3.4.1 | Flaws in Gas Temperature Differential Experiments | 23 |
| 3.4.2 | Frequency Characteristics of Plumes | 24 |
| Chapter 4 | Algorithm Methodology | 30 |
| 4.1 | Basic Framework | 30 |
| 4.2 | Algorithm Structure | 31 |
| 4.2.1 | Application of Highpass Filter | 33 |
| 4.2.2 | Computing Signal Strength | 35 |
| 4.2.3 | Data Spikes and Noise | 36 |

4.2.4 Shimmer Effect . . . 40
4.2.5 Plume Coverage Fraction . . . 44

Chapter 5 Low Flow Experiment . . . 45
5.1 Background Motivation . . . 45
5.2 Imaging Distance and Viewing Angle vs Emission Rate . . . 45
5.3 Experimental Setup . . . 47
5.3.1 Viewing Angle Experiment . . . 47
5.3.2 Imaging Distance Experiment . . . 48
5.4 Testing Environment Background . . . 50
5.4.1 Emission Rate Measurement . . . 50

Chapter 6 Algorithm Validation and Experimental Results . . . 51
6.1 Validation of Algorithm to Replicate Expert Abilities . . . 51
6.2 Probability of Emission Detection . . . 52
6.3 Experimental Results . . . 54
6.3.1 Viewing Angle Experiment . . . 54
6.3.2 Imaging Distance Experiment . . . 54

Chapter 7 Conclusions and Future Work . . . 58
7.1 Future Work . . . 58

Bibliography . . . 60

Appendix A Developed Software Packages . . . 68

LIST OF TABLES

2.1 Camera Frame Rate . . . . . . . . . . . . . . . . . . . . . . . . . . . . . . . . . . . . . . . . 14

3.1 Camera Heights and Viewing Angles . . . . . . . . . . . . . . . . . . . . . . . . . . . . . . 19
3.2 Normalized Standard Deviation Analysis . . . . . . . . . . . . . . . . . . . . . . . . . . . 29

5.1 Released Market Natural Gas Composition . . . . . . . . . . . . . . . . . . . . . . . . . 48

6.1 Expert Evaluation Summary . . . . . . . . . . . . . . . . . . . . . . . . . . . . . . . . . . 51
6.2 Probability of Emission Detection . . . . . . . . . . . . . . . . . . . . . . . . . . . . . . 52

LIST OF FIGURES


2.1 Methane Transmission Fraction vs Wavelength . . . . . . . . . . . . . . . . . . . . . . 10
2.2 Radiative Flow . . . . . . . . . . . . . . . . . . . . . . . . . . . . . . . . . . . . . . 11
2.3 Camera Control Program User Interface . . . . . . . . . . . . . . . . . . . . . . . . . 14
2.4 Data Processing Pipeline . . . . . . . . . . . . . . . . . . . . . . . . . . . . . . . . . 15

3.1 Framework of Gas Temperature Differential Experiment . . . . . . . . . . . . . . . . . 18
3.2 Gas Temperature Differential Experiment Imaging Background Control . . . . . . . . . 20
3.3 Mechanical View of Plume Temperature Control Unit . . . . . . . . . . . . . . . . . . . 21
3.4 Plume Temperature Control Unit Wiring Diagram . . . . . . . . . . . . . . . . . . . . . 22
3.5 Camera Wiring Configuration . . . . . . . . . . . . . . . . . . . . . . . . . . . . . . . 23
3.6 Preliminary Experiments Emission Rate Flaw . . . . . . . . . . . . . . . . . . . . . . . 24
3.7 Pixel Value Analysis . . . . . . . . . . . . . . . . . . . . . . . . . . . . . . . . . . . . 26
3.8 Highpass Filter Effect of Grass Pixels . . . . . . . . . . . . . . . . . . . . . . . . . . 27
3.9 Highpass Filter Effect of Dirt Pixels . . . . . . . . . . . . . . . . . . . . . . . . . . . 28

4.1 Block Diagram of Plume Signal Extraction Algorithm . . . . . . . . . . . . . . . . . . . 31
4.2 Pixel Array Structure . . . . . . . . . . . . . . . . . . . . . . . . . . . . . . . . . . . 32
4.3 Raw Apparent Temperature View of Emission . . . . . . . . . . . . . . . . . . . . . . . 32
4.4 Magnitude Frequency Response Curve . . . . . . . . . . . . . . . . . . . . . . . . . . . 33
4.5 Power Spectra of the Apparent Temperature Signal . . . . . . . . . . . . . . . . . . . . 34
4.6 Standard Deviation Array . . . . . . . . . . . . . . . . . . . . . . . . . . . . . . . . . 35
4.7 Elimination of Noise Floor . . . . . . . . . . . . . . . . . . . . . . . . . . . . . . . . 37
4.8 Raw Standard Deviation Array - Surface . . . . . . . . . . . . . . . . . . . . . . . . . 38
4.9 Blurred Standard Deviation Array - Surface . . . . . . . . . . . . . . . . . . . . . . . 39
4.10 2D Filter Effect - 0.05 - Surface . . . . . . . . . . . . . . . . . . . . . . . . . . . . 40
4.11 2D Filter Effect - 0.2 - Surface . . . . . . . . . . . . . . . . . . . . . . . . . . . . . 41
4.12 2D Filter Effect - 0.1 - Surface . . . . . . . . . . . . . . . . . . . . . . . . . . . . . 42
4.13 Noise threshold CDF . . . . . . . . . . . . . . . . . . . . . . . . . . . . . . . . . . . 43
4.14 Weighted Array Effect . . . . . . . . . . . . . . . . . . . . . . . . . . . . . . . . . . 43

5.1 Low Flow Experiment Overall Framework . . . . . . . . . . . . . . . . . . . . . . . . . 46
5.2 Viewing Angle vs Emission Rate Experimental Setup . . . . . . . . . . . . . . . . . . . 48
5.3 Imaging Distance vs Emission Rate Experimental Setup . . . . . . . . . . . . . . . . . 49

6.1 Probability of Emission Detection - Logistic Regression . . . . . . . . . . . . . . . . . 53
6.2 Viewing Angle vs Emission Rate - Camera 0 Viewing Angle . . . . . . . . . . . . . . . 55
6.3 Viewing Angle vs. Emission Rate . . . . . . . . . . . . . . . . . . . . . . . . . . . . . 56
6.4 Imaging Distance vs. Emission Rate . . . . . . . . . . . . . . . . . . . . . . . . . . . . 57

# Chapter 1

# Introduction

## 1.1 Motivation

Natural gas accounted for approximately 31% of the electricity generated in the United States in 2018, a 26% increase since 2005 [1]. This production was the second highest recorded amount since the record high in 2015. More efficient and effective drilling techniques have increased the domestic production of natural gas. This uptick in production has consequently led to a drop in the price of natural gas, leading to a further increase in the consumption by the industrial and electric power sectors [2–8]. Natural gas is made up a variety of hydrocarbons, with methane ($CH_4$) typically having a mole fraction of 0.939 for market natural gas [9].

Natural gas is starting to be seen as a more environmentally-friendly fossil fuel; it produces lower $CO_2$ emissions per unit energy when combusted than petroleum and coal. However, since methane is a more potent greenhouse gas (GHG) than $CO_2$, with a global warming potential 84-86 times that of carbon dioxide over a 20-year period [10, 11], the benefits of switching to natural gas for the environment greatly depends on the amount of methane emitted unburned from the natural gas supply chain. About 25% of $CH_4$ emissions in the United States originates from the oil and gas industry [12, 13]. A growing number of studies have found the Environmental Protection Agency (EPA) may have underestimated methane emissions [14–18] in its GHG emissions inventory. Some recent estimates of emission rates have gone so far as to debate whether there is a greenhouse gas advantage when switching to natural gas from coal, stating it is possible that methane emissions from natural gas emissions can outweigh the increased combustion $CO_2$ emissions from burning coal. It was found that if more than 3.2% of natural gas is emitted uncombusted between extraction to end use, the environmental impact would be greater than that of coal [19–23].

## 1.2 Optical Gas Imaging Background

To mitigate the environmental impacts of natural gas emissions multiple regulatory agencies require regular emission inspections of natural gas infrastructure, including national [24, 25] and state agencies [26–28]. Inspections are performed using a variety of methods, including periodic surveys using optical gas imaging (OGI) cameras [29]. The most common OGI detection technology utilizes infrared (IR) video cameras filtered to the 3.2-3.4 $\mu$m wavelength, a frequency range where methane has several absorption lines [30–32]. In good conditions, absorptive and emissive gas plumes appearing darker and lighter than surrounding areas, respectively, when viewed in a gray-scale IR video image. Emission detection surveys are typically performed by a trained operator using a handheld video camera. The operator images each component on a facility, and if emissions appear visible in the video image, the operator notes the emission location. Emission detection protocols vary between companies and industry segments. Often camera operators will perform small repairs while noting the location of large problems for repair by other teams.

OGI camera output is affected by environmental conditions, emission survey practices, emission rate/size, emission temperature and gas composition [31, 33]. Challenges include: (1) survey quality varies for each unique OGI operator [34, 35], (2) positive emission identification depends on operator's judgment [36], and (3) assessments of OGI surveys in field conditions seldom have a sufficiently controlled or characterized emissions to make objective measurements of efficacy.

To improve OGI technology, some studies looked at the consistency and accuracy of OGI cameras [35]. Survey environmental conditions such as differential temperature (apparent background minus apparent gas temperature) [31], wind speed and wind direction also impact camera output factors.

Ravikumar et al. states that, while many oil and gas companies use this technology, systematic scientific experimental analysis of the performance of this technology is lacking [31]. Research has been conducted to computationally create a metric to represent the camera output in various environmental conditions. Recent work empirically derived detection probability-of-detection (POD) curves for OGI emission detection in pseudo-realistic conditions and reported a power-law relationship for detection probability and imaging distance [36] when imaging in high sensitivity mode (HSM), a proprietary video processing technique to enhance plume movement for a 5x increase in emission detectability [37].

## 1.3 Related Computational OGI Detection Work

### 1.3.1 Smoke Detection

Several authors in the image processing and computer vision fields have studied and reported on smoke detection methods. Natural gas and smoke plume have similar characteristics. Some simple similarities between the two are dispersion, irregular movements, contrast blending in time, and turbulent fluid motion. Previous work has hypothesized a direct relationship between the transport characteristics of natural gas (methane) and that of smoke [38].

The defining difference between the two fields is the camera utilized to image the plumes. As previously mentioned, methane plumes can be recorded with a mid-IR OGI camera that stores apparent temperature data for each pixel in time. The playback software then scales the apparent temperature data to a grayscale image. In contrast, in smoke detection typical RGB (red, green, blue) colors can be captured and played back in the visible spectral range.

Previous image-based smoke emission detection techniques are explored here and their concepts can be tied back to methane emission detection. Analyzing a single frame or multiple frames in chronological sequence allows for the use of the color modeling, change detection, and texture analysis in smoke detection.

Color modeling is the most primitive and simple form of image processing and fundamentally functions off the inherent idea that smoke is typically gray in color. Color models use color differences to identify smoke-colored pixels [39, 40]. When a pixel has a grayish color, it is marked as positive smoke identification. This method is challenged by backgrounds containing gray objects, as anything gray in the cameras field of view will also be falsely identified as smoke.

Changing detection [41] identifies non-stationary objects in an image to note the region in the field of view for further processing analysis. Background subtraction, a frequently used technique, creates an average background image for frames when there are no moving objects, then subtracts this image from the current image, i.e. the moving frame, to produce a final residual image that contains only the portion of the frame that is in motion. If a pixel value is greater than any set threshold value, that pixel is then marked as smoke signal. A binary mask can be overlaid on the original frame to visually show where signal is detected. If any unique movements occur in the camera's field of view, those movements may be incorrectly identified as smoke.

Texture analysis is a more sophisticated approach when compared to the preceding methods. Texture energy quantitatively describes the perceived amount of texture in an image or a series of images by assessing the amount of variation between neighboring pixel values throughout a series of images or a single image. One approach applies a wavelet transform to identify defining features. The internal shape of the identified features would then be marked as the smoke detection signal [42, 43].

Due to the complex fluctuations in color, shape, and texture occurring in smoke, a more robust system was desired. Multiple studies developed convolutional neural networks (CNN) using machine vision. The model is essentially trained with a large data set of images with the smoke pixel locations known. Given enough training, the model will identify smoke pixel locations [44–46], but the generalizablity of a trained CNN is highly dependent on the breadth and quality of the training data set.

### 1.3.2 OGI Deep Learning

The strong visual relationship between methane and smoke emissions would suggest that a small jump in detection methodology would produce superior OGI detection capabilities. However, this is not the case. Development of deep learning models in OGI emission detection is fairly scarce.

With the objective of creating an autonomous "leak/no leak" detection method, Jingfan et al. has proposed a CNN machine learning model to estimate and detect OGI natural gas emissions by taking a similar approach as the CNN smoke detection models. In this work, they first collect a large number of labeled video frames of methane emissions from different equipment with a range of emission sizes (5.3-2051.6 g $CH_4/h$) and imaging distances (4.6-15.6 m). Using the previously described primitive background subtraction methods, they extract the methane plume from the background. Finally, they compare the results of the developed deep learning model to that of the background subtraction method. The deep learning model performed with overall emission detection accuracy of 95% across all tested emission rates and imaging distances [33].

The Southwest Research Institute developed a machine learning liquid hydrocarbon optical imaging identification model called Smart LEak Detection (SLED) to detect the small emissions (less than 1% of throughput of pipeline) occurring throughout a pipeline. The group is now applying a similar model to identify the gaseous hydrocarbon, methane, called Smart Methane LEak Detection (SLED/M). The model was trained by various emission rates (3-500 SCFH), line pressure (30-210 psig), orifice sizes, (1/32" - 1/8"), and emission geometries (open nozzles, diffuse tubing, and emissioning joints). To simplify, the model algorithm consists of three steps: (1) preprocessing imagery, (2) feature learning and methane detection with convolutional segmentation neural network, then (3) threshold the output with a clustering algorithm. The group suggested potential benefits of the systems, however a quantitative report of "leak/no leak" accuracy is lacking [47].

Deep learning approaches are fundamentally flawed in that the user has no easily accessible information in the steps and/or decision process the model is taking. An emission detection algorithm that can not only identify the presence of the an emission, but additionally assess the camera output is desired.

### 1.3.3 Commercial Products

Autonomous emission detection is very complex. Currently, there are very few OGI based commercial products available. ExxonMobil Research Qatar in cooperation with Providence Photonics developed a Remote Gas Detection technology FLIR™ IR camera add-on called IntelliRed™. This system was created to act as an early warning system to signal operations staff of fugitive gas emissions. IntelliRed™ functions with two IR cameras with one viewing the background FOV and one tuned to view the hydrocarbon and background FOV. IntelliRed™ then calculates this difference in camera outputs to report the presence of an emission [48].

A Honeywell owned company, Rebellion Photonics, developed Gas Cloud Imaging technology (GCI) to continually monitor, record, and analyze footage for the presence of gas emissions, fires, and intruders. This proprietary hyperspectral imaging technology called 'PEARL™' (Physics Enhanced Artificial Intelligence Real-time Logic) uses artificial intelligence paired with the GCI camera technology to detect, identify, and quantify over 47+ gases in real time [49], however no peer-reviewed performance measurements have been published.

FLIR™ Systems in partnership with Providence Photonics announced in late 2017 the development of a Quantitative Optical Gas Imaging (qOGI) technology that was developed to work exclusively with the FLIR™ GF-Series cameras. Providence Photonics' QL320 portable display claims to have the ability to process live video feed from the FLIR™ GF-Series cameras to quantify and output the volumetric and mass emission rates to camera operators [50]. However, performance is unknown, as no peer-reviewed results have been published.

All of the above algorithms are proprietary, making it difficult to use these methods as a common, open-source method of identifying the size and detectability of natural gas emission plumes. In addition, the author knows of no OGI-based emission detection algorithms or models that focus on the time-domain frequency of plume images as a means of plume identification.

### 1.3.4 Predictive Models

Arvind et al. developed a Gaussian dispersion model that recreates IR images for controlled methane release experiments and state expected minimum emission rate detection limits. From this model, the group was able to report specific techniques on how to best see the plume and provide information on the optimal environmental conditions as well as how differential temperature affects plume visibility. However, this work is lacking in the analyzing the effect these variables have on OGI cameras [31, 51].

Some methods utilize a response factor (RF) to determine the visibility of specific emission compounds when compared to another or reference compound. The operator can then calibrate the camera to optimally image a specific gas composition emission. Zeng et al. proposed two new methods in determining RF values. The first method uses a theoretical approach using the radiative transfer equation to derive a relationship for RF with respect to the emission concentration multiplied by the depth of the plume for various gas compounds. The second method validated the theoretical approach with an experimental setup to compare the RF values of methane and propylene relative to propane [52].

## 1.4 Objective and Overview

Previous studies of OGI methods in controlled conditions have focused primarily on camera output. The weakness of these studies is that they relied on a camera operator's judgment to determine if a leak was visible. Therefore, the dependent variable (detection) of these studies was fundamentally qualitative [34–36]. Field studies include both camera and operator performance in the assessment, but since these studies occurred outside a controlled experimental environment where leak location and size are known, the complete identification of all leaks is uncertain, and quantification of leak size is also problematic [53]. While valuable, this type of study is dependent on the limited range of environmental conditions experienced during the study and the experience and performance of the camera operators who participated, and are therefore difficult to replicate and generalize [54].

This work addresses these two challenges by developing a novel, frequency-based algorithm that measures the fraction of the cameras field of view (FOV) where an emission is visible. With the algorithm, this study has the ability to (1) remove the camera operators judgment in assessing emission visibility, (2) ground these previous studies with an algorithm independent of human judgment, and (3) experimentally control variables (gas on/off times), and use this information to provide an unambiguous, algorithmic, metric that is a robust surrogate for "visibility of the emission."

The work is organized as follows:

Chapter 2: *OGI Fundamentals*, describes how the OGI cameras work and how the data was collected and exported during experimentation.

Chapter 3: *Gas Temperature Differential and Camera Background Experiment*, describes the preliminary gas temperature differential experiment to gather and analyze data on the effect of environmental conditions on plume visibility. These experiments also supported development of the experimental setup and improvement in experimental methods. Gas temperature differential experiments 1 (March 27th, 2019), 2 (July 14th, 2019), and 3 (July 21st, 2019) occurred on different days to capture different weather conditions. These three experiments will be referred to as preliminary experiments.

Chapter 4: *Algorithm Methodology*, explains the methodology used to build the frequency-based plume extraction algorithm to distinguish plumes from backgrounds in video streams.

Chapter 5: *Low Flow Experiment*, discuses an experiment at lower flow rates for viewing angle, emission rate, and imaging distance investigations. Viewing angle experiment (November 14th, 2019) and imaging distance experiment (January 28, 2020) occurred on different days.

Chapter 6: *Algorithm Validation and Experimental Results*, presents the algorithm validation and experimental results.

Chapter 7: *Conclusions and Future Work*, concludes on the plume extraction algorithm and offers a recommendation for future work.

In this work, wind bearing is defined as degrees from north in the direction the wind is coming from. Released market natural gas was directly measured in standard cubic feet per hour (SCFH) then converted to grams per hour (g/h) (1 SCFH = 21.8 g/h).

# Chapter 2

# OGI Fundamentals

## 2.1 Infrared Fundamentals and Imaging Properties

In 2012 the United States Environmental Protection Agency (EPA) updated the New Source Performance Standards (NSPS) allowing all oil and gas operators to use OGI [24] as an alternative to EPA Method 21 as an emission detection method in upstream and midstream sectors of the natural gas supply chain [55]. To evaluate the performance of OGI, a deeper understanding of how they function is necessary.

### 2.1.1 Infrared Fundamentals

OGI cameras utilize the principal of light absorption by gases at specific wavelengths. Looking at methane because it is the primary constituent of natural gas, the molecule is made up of one carbon and four hydrogen atoms $(CH_4)$. This molecule has 15 degrees of freedom (vibration along an axis, rotation, twisting, stretching, rocking, wagging, etc), and constantly transitions from one movement state to the next at a certain frequency. This process can be described by the Beer Lambert Law, as shown in Equation (2.1), where $K_\alpha$ is the molar absorption cross-section, $\rho$ is the concentration path length, and $I_t$ and $I_0$ are the transmitted and incident light intensity, respectively [30, 31].

$$\frac{I_t}{I_0} = e^{-K_\alpha \cdot \rho} \tag{2.1}$$

When the frequency of these transitions is equal to a frequency of light, that frequency is then absorbed by the molecule. For the purposes of mid-IR imaging, methane transitions at a frequency of $9.090 \cdot 10^{13}\ Hz$ or $3.3\mu m$.

Figure 2.1 was derived by experimentally measuring the effect of the Beer Lambert Law to visually show how the transmissivity of methane is effected by various wavelengths [32]. By definition transmissivity is inversely proportional to absorptivity. In order to maximize the contrast of the methane plume relative to background, OGI cameras view a spectral range of light with a wavelength of 3.2-3.4 $\mu$m [30,56], effectively concentrating the camera's response on wavelengths with strong absorptivity.

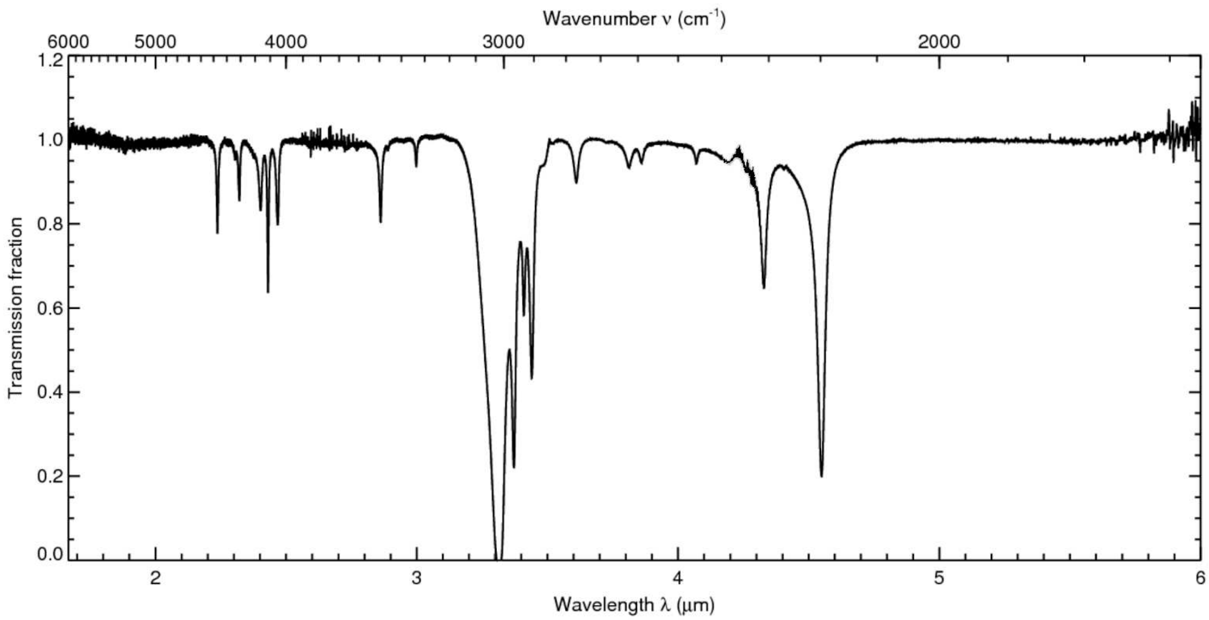


**Figure 2.1:** Transmission vs wavelength of methane which peaks in absorptivity (inverse of transmissivity) around 3.2-3.4 $\mu$m. Adopted from [32]

.

OGI cameras' focal plane sensors and optical systems are tuned to view spectral light at the desired wavelength range. Methane imaging OGI camera sensors are typically cooled (77K is common) with a helium-based Stirling cycle cooler to increase the detected signal/noise ratio for optimal plume viewing [57].

### 2.1.2 Imaging Properties

An infrared camera responds to incident radiation in the camera's field of view (FOV). Incident radiation on the camera sensor originates from three phenomena: (1) direct thermal (light emitted from gas plume), (2) reflected (light reflected off the plume) and (3) transmitted irradiation (unabsorbed light from the background temperature). These three radiative factors are effected by the emissivity, reflectivity and transmissivity, respectively, of the scene [58].

The combination of the three modes of irradiation create a photocurrent in the cryogenic detector of the camera proportional to irradiation intensity for each pixel, in the wavelength range set by the filters in the camera. The relative pixel signal is normalized and internally converted to an apparent temperature. The extraction of this apparent temperature data is essential for the remainder of this work and is further discussed in the following section [59].

If a gas cloud is in the FOV between the camera and the background, and it absorbs radiation in the camera spectral range, the amount of incident radiation to the detector will decrease. Radiant contrast between the gas and the background is required, therefore there must be an apparent temperature difference between the gas and the background. A simplified model showing the effect of gas in the FOV can be seen in Figure 2.2.

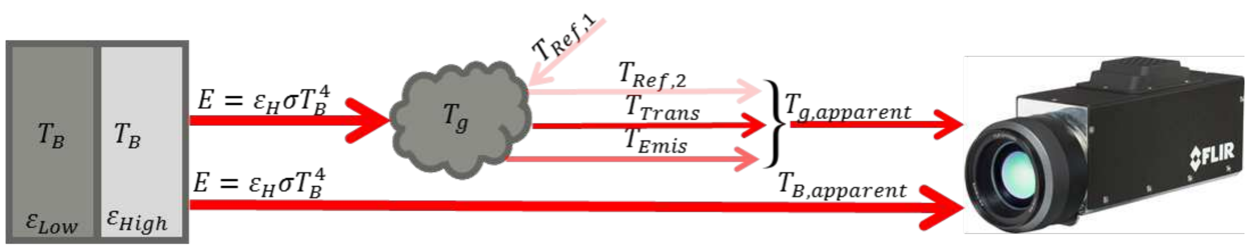


**Figure 2.2:** Diagram of transmissive, emissive, and reflective radiative flows when passing through a plume. Background radiation not absorbed by gas becomes transmitted irradiation. Gas temperature emits emissive radiation. Surrounding radiation reflected off plume becomes reflected incident radiation. Various background emissivities exist. For plume to be visible, $T_{g,apparent} \neq T_{B,apparent}$.

Another important factor that needs to be addressed to have optimal imaging from the OGI camera is the focus. The FLIR™ G300a camera has a sensor-based autofocus system. This system's technology uses the camera's sensor for both focus and image recording. The autofocus procedure is done by changing the lens position and assessing contrast. While the exact method used by the G300a cameras is unknown, typically a 'texture energy' method is utilized, similar to that described earlier for smoke detection (Section 1.3.1). The lens position that provides highest contrast is used as the correct focus position. To speed-up the autofocus procedure, the autofocus is done in two steps. The first runs over the full range of the lenses movement with a significant step size, which will provide the estimated position for the second second run, which runs over the smaller range with a small step size. The camera's lens position may also be adjusted manually on the G300a [30].

## 2.2 Description of Data Acquisition

The experiments in this study used six tripod mounted FLIR™ G300a OGI cameras with a 14.5° fixed lens, 320 x 240 pixel IR resolution, 14.5° x 10.8° FOV, and a 38 mm focal length. The cameras were hard-wired to a control computer to be controlled simultaneously, and had no human interface. Camera wiring configuration is further discussed in Section 3.3.3

All experiments for this work were conducted at the Methane Emissions Technology and Evaluation Center (METEC) in Fort Collins, Colorado. METEC simulates natural gas emissions as they may occur in the field to test/train/qualify operators and emission detection solutions. Equipment at METEC includes well heads, dehydrators, compressors etc. This equipment was plumbed with 1/4" steel tubing to create controlled methane or market natural gas emissions through the use of pressure regulators, choked flow orifices, and thermal mass flow meters (MFM) [60].

As previously noted, qualitative emission detection studies have used the FLIR™ GF320 OGI camera [36, 51]. The FLIR™ G300a camera and FLIR™ GF320 camera fundamentally function identically, however, the GF320 is a handheld device that is meant for operator controlled detection and features a user interface for direct, live emission viewing. The FLIR™ G300a requires an external computer power source and hard drive to store recordings. The section discusses the software required to control the camera and the data processing pipeline required to capture and analyze an OGI recording.

### 2.2.1 Development of Imaging Software

While OGI cameras are typically used individually, the use of multiple cameras in this work required the development of data acquisition software to control all six cameras together. While the computer commands all cameras to start recording simultaneously, the cameras are not externally synchronized and, due to communication and computation delays, there are always some time difference between frames from each camera. The frame rate of the camera is approximately 10 Hz (100 ms per frame). Assuming an effective communication and control rate of 9600 baud, timing errors would be $\approx$60 ms between cameras when starting or ending a recording. This translates to differences in scene recording that is a fraction (60% nominal) of the cameras' framerate.

Videos were saved using the FLIR™ Atlas Software Development Kit (SDK) for .NET™, producing sequence (*.*SEQ*) files. Sequence files output video images as frames of apparent temperature per pixel. These were imported into MATLAB® for analysis.

Recording an emission point with multiple cameras recording (approximately) simultaneously supports analysis of how environmental variables affect the image without the uncertainty of changing environmental variables as one camera is moved into different viewing positions. With this idea in mind, a camera control program was developed to view, record, and save the video feed from each camera. Figure 2.3 shows a direct emission point from six viewing angles.

The FLIR™ G300a manual states the cameras record at a nominal rate of 10 frames per second (fps). However, the frame rate of the cameras varies between cameras. The mean and standard deviation frame rate of three recordings for each camera were calculated by noting the number of recorded frames and dividing by the true length of the recording taken from the sequence file meta data. As shown in Figure 2.1, the frame rate is typically closer to 9 fps for all cameras.

**Figure 2.3:** Screen shot of the camera control program. The recording interface shows one emission point (the pipe in the lower center of each panel) imaged from multiple viewpoints.

**Table 2.1:** Measured frame rate of each camera

| Camera | Mean (fps) | Standard Deviation (fps)) | Range (fps) |
|---|---|---|---|
| 0 | 9.21 | 0.121 | 0.136 |
| 1 | 9.11 | 0.025 | 0.028 |
| 2 | 9.00 | 0.079 | 0.081 |
| 3 | 9.04 | 0.066 | 0.070 |
| 4 | 9.22 | 0.051 | 0.053 |
| 5 | 9.18 | 0.049 | 0.056 |

### 2.2.2 Data Processing Pipeline

The analysis requires the apparent temperature value for each pixel in each frame. These data are transformed into MATLAB® file format via the steps described in Figure 2.4.

In this work, the extraction of all apparent temperature pixel values in each frame was completed through software, "ExportTool," developed by CSU. This program iteratively extracts the desired apparent temperature data and exports it to a more common, comma-separated values (CSV) file format.

The final step in the pipeline converts the CSV to a three dimensional MATLAB® array. This is accomplished by importing the file to the MATLAB® workspace with the *csvread* function then


**Figure 2.4:** Visual representation of required steps to export a recordings to the necessary MATLAB® file format

restructuring the array. The resulting data array is 240 by 320 by the number of frames in a recording. Further analysis of this array is described in 4, Algorithm Methodology.

For all experiments in this study, recordings consist of a 60 s recording with the emission point releasing gas ("gas on phase") directly followed by a 30 s record with the emission point releasing no gas ("gas off phase"). These periods were identified and trimmed by frames 1-550 ( 60 s) for the gas on phase and frames 650-end ( 25 s) for the gas off phase.

# Chapter 3

# Gas Temperature Differential and Camera Background Experiment

This chapter discusses the preliminary experiments used to analyze the effect that environmental conditions have on recorded videos. Although no empirical results are derived from the preliminary experiments, a crucial discovery in algorithm development is discussed.

Previous work defined differential temperature as plume apparent temperature minus background apparent temperature. To distinguish between apparent temperature and the temperature of the gas being released, the *gas temperature differential* (GTD) is defined as *measured* plume temperature minus *measured* ambient air temperature.

## 3.1 Background Motivation

Previous computational predictive models quantified the effect of environmental conditions, such as imaging distance, differential temperature, scene temperature, and emissivity on camera response while imaging an emission [31, 51]. The GTD experiments described in this chapter focused on two of these analyzed environmental conditions, gas temperature differential and camera imaging background.

Differential temperature was defined as the difference in apparent temperature between the plume and the background, or 'scene': $\Delta T = T_p - T_s$, where $\Delta T$ is the apparent temperature differential, $T_p$ is the plume apparent temperature, and $T_s$ is the scene apparent temperature. It was found that the likelihood of detection increases when the apparent background temperature is warmer than the plume apparent temperature, but it was noted that this effect is less than other tested variables [31, 51].

Ravikumar et al. analyzed the effect of emissivity on camera detection effectiveness and suggests that low emissive scenes will provide greater contrast than high emissive scenes. In surveys, scenes with objects in the field of view like forests or grass fields will generally have higher emissivities when compared to metallic surfaces [31]. It is well known that the scenes with movements or high complexity (high texture energy) effect the likelihood of positive operator emission detection.

The current work takes a similar, but experimental approach. A realistic background scene will not have constant apparent temperature to compare to plume apparent temperature, therefore, this work compares plume gas temperature to ambient air temperature (GTD). By pairing the imaging background variables of varying emissivity and imaging complexity, various imaging background scenarios were tested and are discussed in the following section. The objective of this preliminary experiment is to determine how the two independent variables (1) GTD, and (2) image background effects the camera output.

## 3.2 Gas Temperature Differential Design of Experiment

The gaps is previous research stimulated interest in performing analysis of how GTD between the gas plume and background impact camera imaging. The focus of this study is developing a quantitative measure of OGI camera output in detecting emissions with varying background conditions and varying GTD values. The experimental plan is illustrated in Figure 3.1.

The experiment controls three variables.

- *Backgrounds:* To account for various wind direction shifts throughout the experiment day, the six cameras were divided into two, three-camera, clusters with a controlled emission in the field of view. The three cameras in each cluster view emission location against backgrounds of the sky, sky and ground, and ground, respectively, by varying the height of the cameras.

- *Plume temperature:* GTD is a measure in the difference in plume temperature relative to the ambient air temperature. For each GTD experiment, the GTD is varied in 5 degree increments from -10 to +10 (°C).

| | | | | | | | | |
|---|---|---|---|---|---|---|---|---|
| **Camera Number** | (a) Cluster B | Ground background | 5 | | | | | |
| | | Ground and Sky Background | 4 | | | (b) | | |
| | | Sky Background | 3 | | | | | |
| | Cluster A | Ground background | 2 | | | | | |
| | | Ground and Sky Background | 1 | | | | | |
| | | Sky Background | 0 | | | | | |
| **Temperature Differential [C]** (Plume Temp – Ambient Air Temp) | | | | -10 | -5 | 0 | 5 | 10 |
| Recording Set ID | | | | 1 | 2 | 3 | 4 | 5 |
| | | | | 7 | 6 | 8 | 10 | 9 (c) |
| | | | | 12 | 11 | 14 | 13 | 15 |

**Figure 3.1:** Gas temperature differential design of experiment featuring: (a) Two three-camera clusters A and B looking in orthogonal directions to account for wind shifts; (b) Each empty box representing a recording with the respective set of independent variables; (c) Repeating GTD recordings in randomized order for statistical purposes. This GTD experiment is further repeated 5 times a day, for three separate days (GTD experiment 1, 2, and 3) to gather data for various weather and wind effects.

- *Emission rate:* Emission rate is controlled by a combination of pressure regulators and three solenoid valve orifices to allow for 8 varying emission rates. For each GTD experiment, gas is released for a fixed valve configuration of 544 g/h for a gas on phase directly followed by a gas off phase.

Wind speeds and ambient temperatures were not controlled. For GTD experiment 1, performed on March 27th, 2019, wind speed and direction varied between 1.5 to 4.2 m/s and 78 to 163 N. Temperatures varied between 14 and 21 °C. Conditions for each GTD experiment are summarized in *DataMaster.xlsx*, sheet *PreliminaryExperiments*.

Recordings 7-15 are in a randomized order to avoid any bias due to the order of recordings. A single GTD experiment consists of 15 recording sets and is repeated an additional 4 times to acquire more data to increase confidence in the results. The GTD experiment is repeated two times on different days to create the GTD experiments 1, 2, and 3.

## 3.3 Gas Temperature Differential Experimental Setup

Experimentally controlling the (1) camera background and (2) GTD for the preliminary experiments are described in the following sections. Referring to Figure 3.1, all experiments consist of recording video with the gas on for 60 s, then the gas off for 30 s. The GTD experiment shown in Figure 3.2 was performed on March 27th, 2019 with a gas volume of 544 g/h, and winds from 83 N (from right to left of camera's FOV) at 3.2 m/s.

### 3.3.1 Camera Imaging Background Control

As previously described, the six cameras recording approximately simultaneously allowed for the analysis of the same emission under identical conditions with only difference between the cameras being the angle of view, and therefore the background, and any differences in the sensitivity of the camera itself.

Figure 3.2 shows the experimental setup. The camera setup consists of two three-camera clusters surrounding the emission-point. Cluster A consists of three cameras at approximately the same distance and angle from the emission-point but vary in height. Camera 0 is closest to the ground, camera 1 is level with the emission-point, and camera 2 is the highest with the cameras looking at the sky, sky and ground, and ground respectively.

**Table 3.1:** A summary of all camera heights, viewing angles, and imaging background

| Cluster | Camera # | Height [m] | Viewing Angle | Imaging Background |
|---|---|---|---|---|
| A | 0 | 0.42 | North | Sky |
| A | 1 | 1.37 | North | Sky and Ground |
| A | 2 | 2.03 | North | Ground |
| B | 3 | 0.42 | East | Sky |
| B | 4 | 1.37 | East | Sky and Ground |
| B | 5 | 2.03 | East | Ground |

Cluster B is viewing the emission location from a direction orthogonal to cluster A to provide two viewpoints with the wind at different angles relative to the viewing direction. Cluster A cameras viewed the emission location from the south, looking north. Custer B viewed the emission

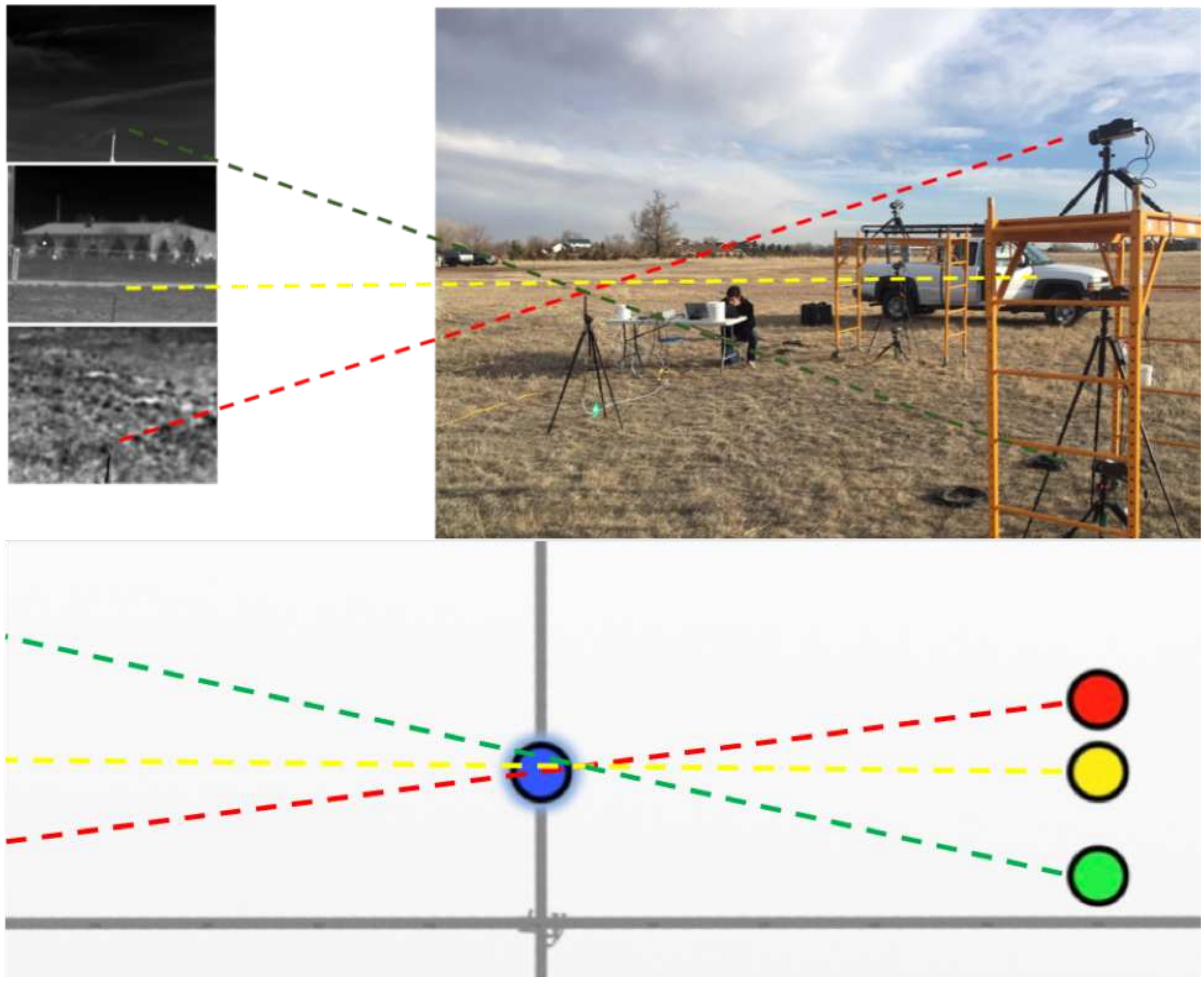

**Figure 3.2:** Upper Figure: Experimental setup during a GTD experiment showing cluster B. Lower Figure: 2D model of camera experimental setup with cameras locations represented as dots. Red-grass background. Yellow-sky and ground background. Green-sky background. Blue-emission point.

from the west, looking east. All cameras are set about 5 m from the emission point. Figure 3.2 visually shows the camera and emission-point setup of a cluster of cameras. Table 3.1 summarized height and viewing angle data for all cameras.

### 3.3.2 Plume Temperature Control Unit

The plume temperature control unit shown in Figure 3.3 was used to control the gas temperature relative to ambient temperature. A 190 W in-line gas heater was used to heat the gas (Autotune PID [61] from Omega Engineering [62], using a K-type thermocouple input). Since the temperature range of the emitted gas also needs to be cooler than the incoming gas temperature, the gas was passed through a copper coil submerged in ice water before entering the in-line heater. The thermocouple is rated for a temperature range of –270 to 1260C and has a standard accuracy of ± 2.2 °C or ± .75% - whichever is highest [63]. During experiments, the controller achieved an indicated gas temperature measurement within ±1 °C. Combined with the thermocouple accuracy, the temperature was therefore controlled to within ±3.2 °C. The thermocouple was positioned about 1 m upstream of the emission point. Figure 3.4 shows a block diagram of the heating unit's wiring.

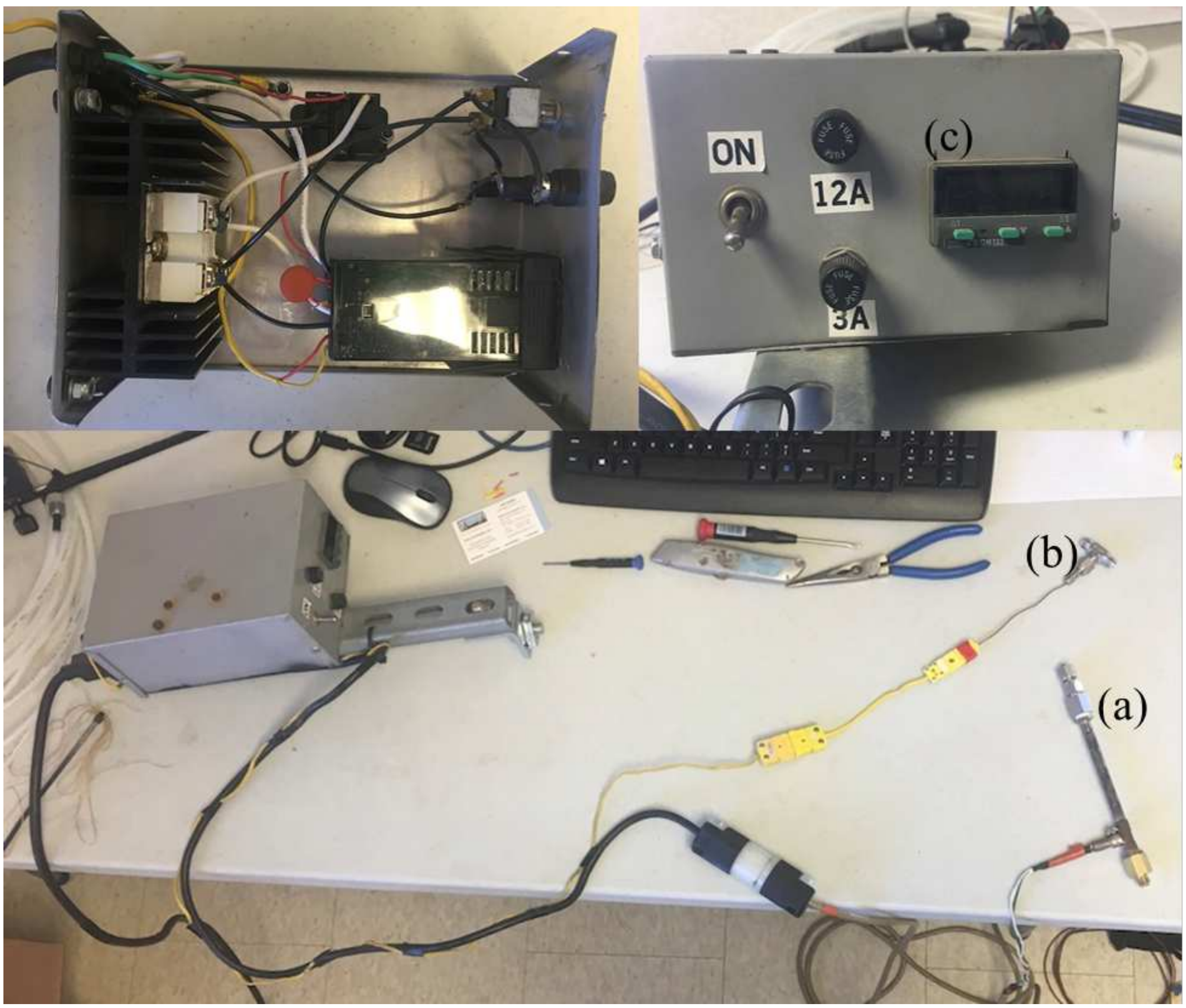


**Figure 3.3:** Mechanical view of the plume temperature control unit featuring an (a) in-line gas heater, (b) type K thermocouple and a (c) PID controller

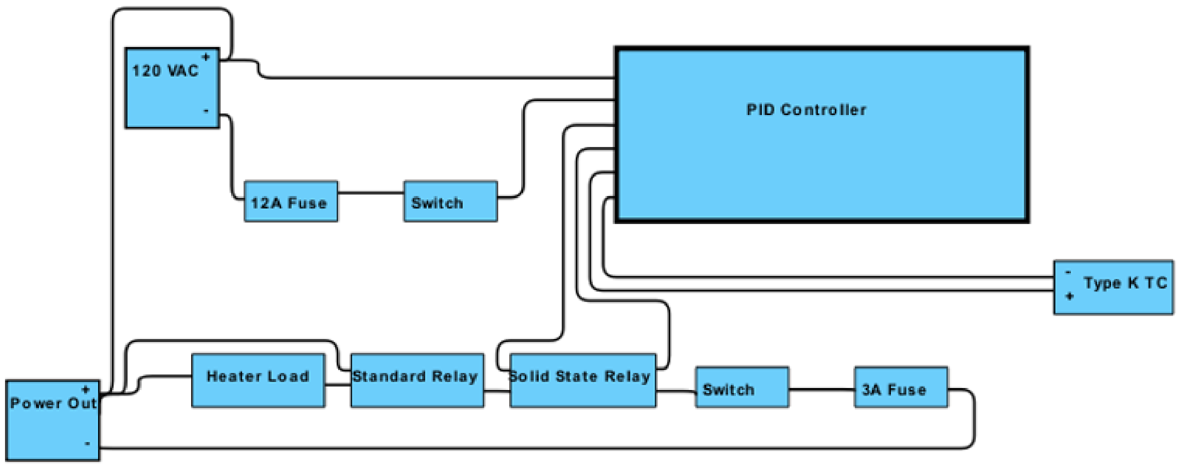


**Figure 3.4:** Wring diagram of the plume temperature control unit featuring an in-line gas heater, type K thermocouple and a PID controller

### 3.3.3 Camera Wiring Configuration

The FLIR™ G300a cameras are powered over Ethernet and transfer image data at approximately 10 Hz, as 8-bit 240x320 pixel video frames. The power over Ethernet (PoE) switch also acts a network hub to connect all cameras to a control computer. To visualize the wiring, a box diagram is shown in Figure 3.5. All connections are:

| Connection | Cable |
|---:|---|
| Controller computer to POE switch | CAT-6 Ethernet |
| POE switch to camera power splitter Data Out port | CAT-6 Ethernet |
| Power splitter Data In port to camera 10/100 port | CAT-6 Ethernet |
| Power splitter 12 VDC power to camera 12/24 VDC port | 12VDC cable |

## 3.4 Inconclusive Quantitative Results

This design of experiment consisted of 180 separate recording sets, with six camera point of views, creating a dataset of 1080 recordings. This section discusses the major flaws in the experimental design as well as what was learned/discovered from the preliminary experiments.

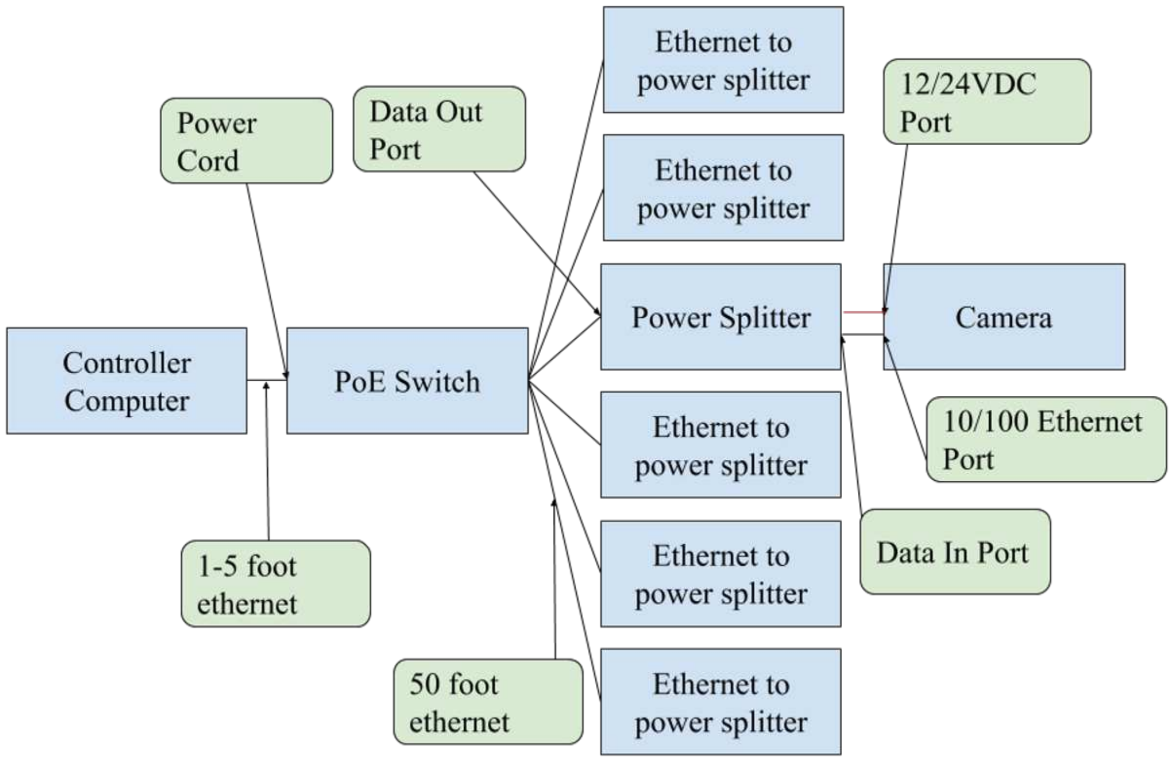


**Figure 3.5:** Wiring diagram to control six FLIR 300a cameras from a single controller computer. The power splitter to camera wiring is repeated for each camera.

### 3.4.1 Flaws in Gas Temperature Differential Experiments

To reiterate, the purpose of the GTD experiment was to analyze the effect GTD and camera viewing angle have on the cameras ability to image the emission. A visual, controlled difference between GTD experiments was expected but not observed, leading to preliminary experiments being scrapped. A few likely reasons of an unobserved effect could be: (1) emission rate was too high for the 5 m imaging distance, and (2) significant error associated with the plume temperature control unit.

As is later discussed in Chapter 4, the developed emission detection parameter develops a metric for plume visibility related to the fraction of the field of view covered by a visible gas plume. The utilized emission rate in all GTD experiments was 544 g/h. At this emission and at an imaging distance of about 5 m, the plume typically extended beyond the camera's field of view before dispersing below visible limits. Figure 3.6 shows a single frame of a recording from camera

0 with a GTD of +5 °C. Wind direction and speed of 85 N and 4.11 m/s, respectively. Recording can be accessed in the file: *SupplementalData.zip*.

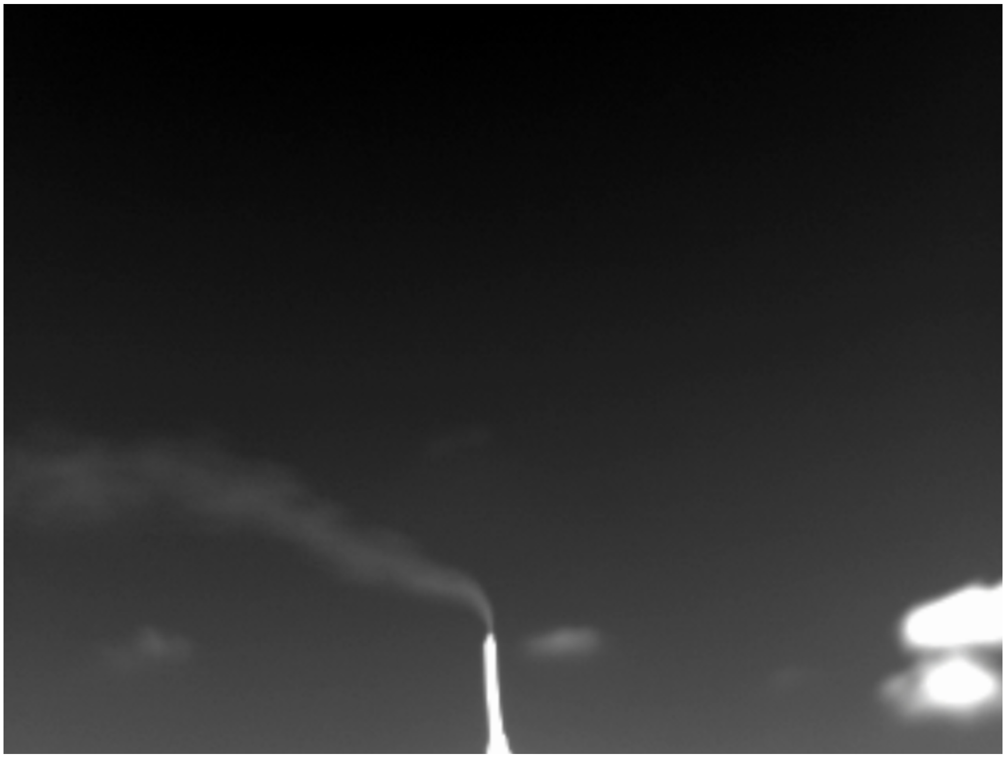

**Figure 3.6:** A single frame of the a recording from camera 0 (sky background facing North) with a GTD of +5 °C. Wind direction and speed of 83 N and 3.25 m/s, respectively.

Providence Photonics performed a study assessing the theoretical minimum detection limits of methane and propane for a range of differential temperatures (apparent plume temperature minus apparent background temperature). They found that as the differential temperature approached zero, the minimum detection limit asymptotically goes to infinity [51]. However, in experimental data collected here, plumes with a GTD of 0 °C were visible, indicating that there was significant *apparent* differential temperature even when GTD was zero.

### 3.4.2 Frequency Characteristics of Plumes

While the temperature differential experiments did not provide data to quantify plume extent, these recordings provided key information relating to the difference in frequency content between pixels inside and outside of the gas plume. An example time series of apparent temperatures for several pixels are shown in Figure 3.7 and marked on a single frame from the video. The pixels were selected to illustrate markedly different backgrounds. Color indicates the type of background – dirt road, grass, or a moving flag – while the box or ‘X’ point shape indicates inside and outside the plume, respectively. The six locations are:

- A highly reflective dirt road:
  - In plume - Red box
  - Outside plume - Red X
- A less reflective, near-field grass location:
  - In plume - Blue box
  - Outside plume - Blue X
- A moving flag in the background:
  - Outside plume - Green X

Due to the wind speed, the grass exhibits a small amount of random motion throughout the video, while the highly reflective road exhibits some random shimmer.

All pixels show a similar pattern of low-frequency drift in apparent temperature, typically $\pm$ 2 °C over the 90 second video. Apparent temperature offsets between pixels are characteristic of this type of imaging, with a dirt road showing as a warmer apparent temperature, grass as cooler, and plume as cooler still. In this frame, the plume is absorptive. Pixels in the gas plume exhibit a significant high-frequency signal superimposed on the low-frequency drift which is not visible in areas outside the plume. The flag has continuous high frequency, high magnitude fluctuations throughout recording.

The low-frequency thermal drift has two likely causes. First, varying atmospheric conditions throughout a 90 s experiment may cause changes in solar irradiation, and therefore changes in

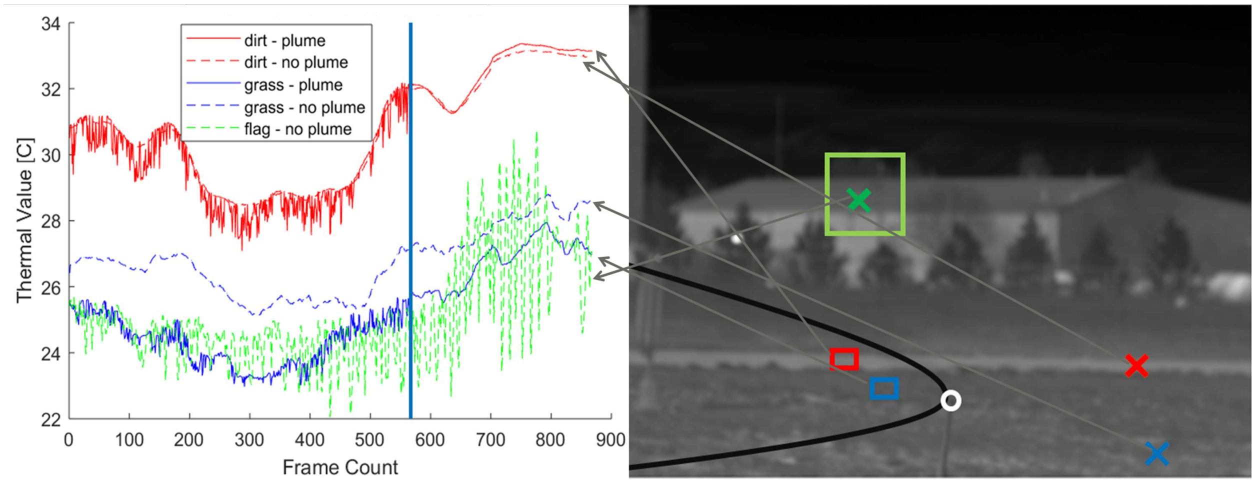


**Figure 3.7:** Example of one still frame from preliminary experiments. Video frames show apparent temperature shown in gray scale from coldest (black) to warmest (white). The apparent temperature range for this scene is 13.9-48.0 °C. The release point is identified by a white circle, and the rough extent of the plume is enclosed in the black curve. A flag near the building is marked with a green box. The plot to the left of the video frame shows a time series of apparent temperature for the five points in the frame – pixels are marked with a box (inside plume) and a 'X' (outside of plume) and colors match lines on the plot. The vertical blue band marks when the gas flow was stopped. See *SupplementalData.zip* for the video.

reflected irradiance and resulting apparent temperature. Second, the camera's internal components may vary in temperature due to drift in the sensor cooling system, creating slowly varying changes in the camera's estimated apparent temperature values [64–66].

Figure 3.7 shows that there is a marked difference in high frequency content for pixels inside the plume relative to pixels outside the plume, provided the pixel is not imaging an object which is moving quickly. To extract the high frequency signal, a high-pas filter was applied. Bandwidth of the time-domain signal is $5\ Hz$ for a 10 fps video rate [67]. A Kaiser window finite impulse response (FIR) high pass filter was used with a cutoff frequency of $2.5\ Hz$, steepness of $0.85$, and stopband attenuation of $60\ dB$ [68], using the MATLAB® Signal Processing Toolbox™. Results are shown in Figure 3.8 and 3.9 for the grass and dirt pixels identified in Figure 3.7.

Comparison of the inside and outside plume pixels provides evidence that pixels inside the plume exhibit substantial high-frequency signal that is not seen in pixels outside the plume. Using the standard deviation of the filtered signal as a measure of the signal strength we compute a normalized signal strength, $\hat{\sigma}$, as:

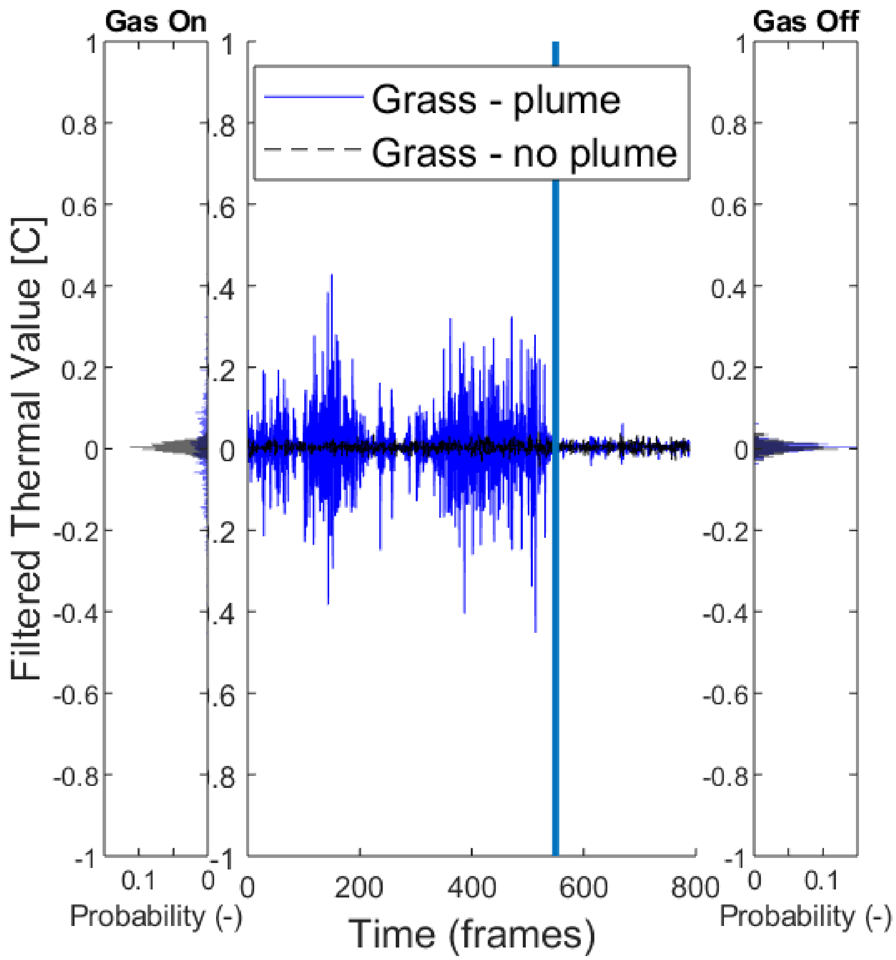


**Figure 3.8:** Highpass filter applied to time series from Figure 3.7. Vertical blue line identifies frame where the gas emission is transitioning from on to off. Colors match those of lines in Figure 3.7. Center plot: Time series of apparent temperature, after filtering, for pixles inside and outside the plume with a grass background. Right plot: Histogram of apparent temperature with gas off. Left plot: Histogram of apparent temperature with gas on.

$$\hat{\sigma} = \frac{\sigma_g}{\sigma_o} \tag{3.1}$$

for each pixel, where $\sigma_g$ is the standard deviation of the filtered signal when the gas is on, and $\sigma_o$ is the standard deviation when the gas is off. For the selected pixels, locations in the plume exhibit substantially larger normalized signal– 25.8 and 8.8 for the road and grass, respectively – versus similar locations outside the plume – 1.1 and 0.92. Extending this analysis to 6 other videos

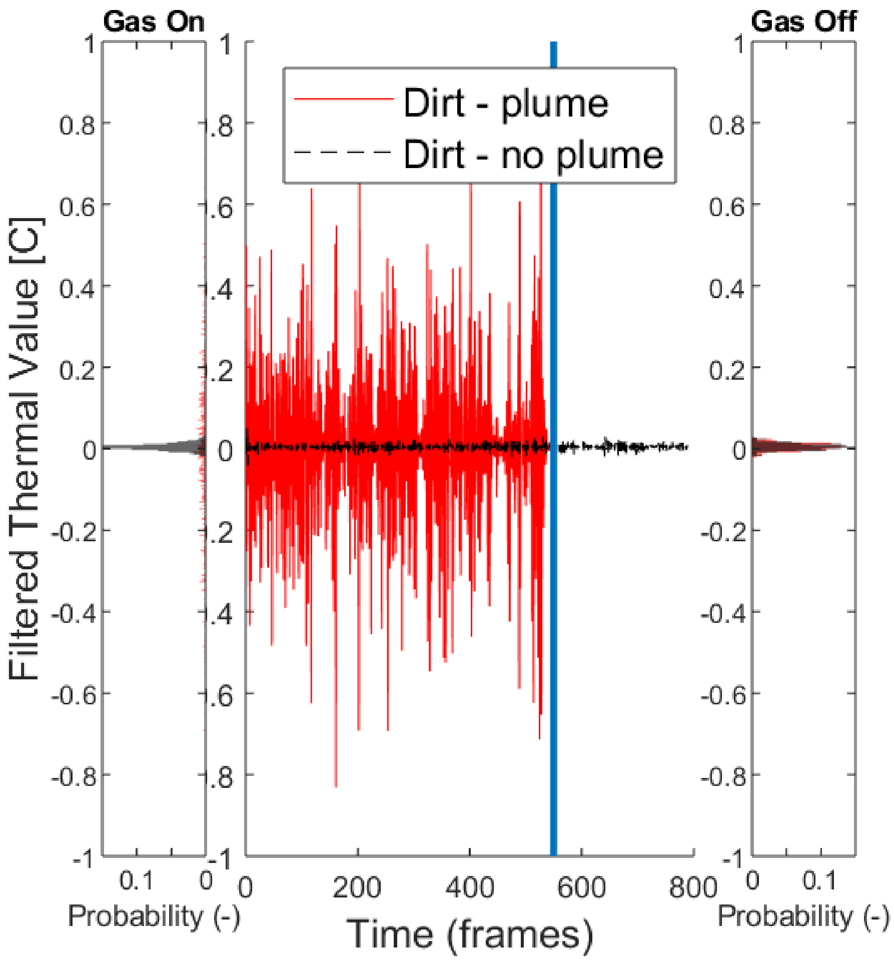


**Figure 3.9:** Highpass filter applied to time series from Figure 3.7. Vertical blue line identifies frame where the gas emission is transitioning from on to off. Colors match those of lines in Figure 3.7. Center plot: Time series of apparent temperature, after filtering, for pixles inside and outside the plume with a dirt background. Right plot: Histogram of apparent temperature with gas off. Left plot: Histogram of apparent temperature with gas on.

taken during preliminary testing, Table 3.2 sampled pixels exhibited similar ratios between inside- and outside-plume pixels.

Preliminary experimentation with the aims of quantifying the effect GTD and camera imaging background proved to be inconclusive, however, a crucial algorithm discovery led to the development of the novel frequency-based plume extraction method. The filtering algorithm method is further discussed in Chapter 4.

**Table 3.2:** Normalized standard deviation study of preliminary recordings.

| Camera | 1 | 1 | 1 | 1 | 1 | 1 |
|---|---|---|---|---|---|---|
| Recording Time | 15:50 | 15:54 | 15:57 | 16:04 | 16:06 | 16:22 |
| Video Set | 1 | 2 | 3 | 4 | 5 | 6 |
| Dirt - Plume | 24.9 | 38.1 | 19.8 | 25.2 | 25.4 | 15.5 |
| Dirt - No Plume | 1.13 | 0.99 | 0.91 | 1.19 | 1.15 | 0.98 |
| Grass - Plume | 8.80 | 4.38 | 5.53 | 11.1 | 10.4 | 4.31 |
| Grass - No Plume | 0.92 | 1.32 | 0.92 | 0.92 | 1.4 | 0.92 |
| Flag | 0.48 | 0.97 | 0.94 | 1.06 | 0.74 | 1.19 |

# Chapter 4

# Algorithm Methodology

This chapter explains the algorithm developed to distinguish plumes from backgrounds in video streams. The following chapter, Chapter 5, describes the application of this algorithm to experiments with lower flow rates than the preliminary GTD experiments. Finally, Chapter 6 explains algorithm validation and experimental results. The algorithm was written in MATLAB® and uses the MATLAB® Signal Processing Toolbox™.

## 4.1 Basic Framework

The underlying assumption behind this algorithm is that the OGI cameras capturing the leak are completely stationary (i.e secured to a tripod). Using this assumption, the developed algorithm should translate to other experimental environments. Additionally, it is assumed that recordings are captured, saved, exported and then post-processed with the developed algorithm. It is not in the scope of this work to create a process for real-time viewing of gas leaks.

With these caveats in mind, the basic function of this algorithm is to extract the unique gas plume signal from the background and to quantitatively report the fraction of the FOV where the plume is visible. While applied here to quantify the probability of detection of a leak, the algorithm has a strong potential to improve OGI emission detection of automated or semi-automated systems. The algorithm represents the core contribution of this work.

Preliminary experiments from Chapter 3 indicated that pixels imaging the gas plume exhibit more high-frequency signal relative to pixels outside the gas plume. The purpose of the proposed algorithm is to identify the gas plume signal while removing any signal from background areas of the scene, and then to develop a quantitative metric that is strongly correlated with the visibility of the plume, where visibility is defined as "identifiable by a trained user in similar conditions at a probability-of-detection (POD) greater than X%."

Figure 4.1 below depicts the block diagram of the algorithm's methodology. First, as described in Subsection 2.2.2, the apparent temperature data is exported to a MATLAB® array format. A high pass filter is then applied in the time direction to attenuate lower frequencies, removing the impact of apparent temperature drift. The standard deviation is then calculated for each pixel data set to compute signal strength. Final algorithm steps reduce false positives. Two-dimensional filtering is used to reduce noise and attenuate data spikes. When viewing natural gas equipment with low emissivity, edges of the equipment have a pronounced "shimmering". These areas are attenuated by removing pixels that show movement (shimmer) in both gas on and gas off phases. Finally, all pixels with a residual value above a set threshold are used to calculate the output parameter, plume coverage fraction.

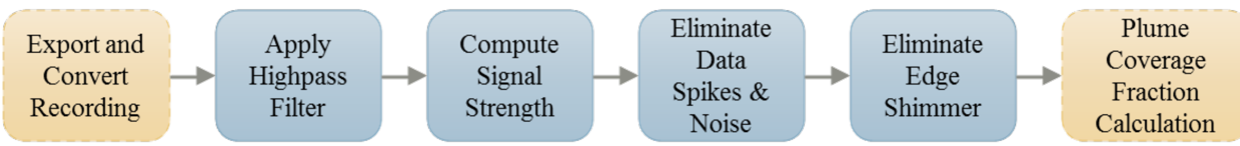


**Figure 4.1:** Block diagram of plume signal extraction algorithm

The algorithm is applied to each recording separately. Each recording, $\boldsymbol{R}$, consisted of a three dimensional array of apparent temperature readings (in °C) consisting of 320 pixels in the $\boldsymbol{i}$ (horizontal) direction, 240 pixels in the $\boldsymbol{j}$ (vertical) direction and $N$ frames in the $\boldsymbol{k}$ (time) direction. The array structure is shown schematically in Figure 4.2. For algorithmic steps that operate on one pixel, such as filtering, the algorithm works in the $\boldsymbol{k}$, i.e. time, direction. Development of summary statistics iterate over all pixels, and use $i, j, k$ indices to uniquely identify each pixel in each frame.

## 4.2 Algorithm Structure

This section explains the steps in the algorithm shown in Figure 4.1. Throughout this process, the information extraction techniques perform calculation on each frame, starting with the raw apparent temperature value array, $\boldsymbol{R}$. To illustrate the effect of each algorithmic step, subsequent figures show the first frame of the array from recordings of a well head that were completed at 13:10

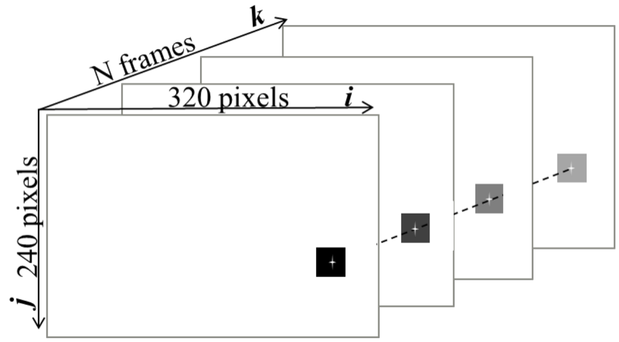


**Figure 4.2:** Visual representation of the pixel array. The $\boldsymbol{i}$ (horizontal) direction has 320 pixels, the $\boldsymbol{j}$ (vertical) 240 pixels, and a typical video recording has 900 frames in the $\boldsymbol{k}$ direction. Four frames as shown for illustration. Pixel is not true size.

of November 14th, 2019. Figure 4.3 shows the starting data, leak rates, environmental conditions and camera viewpoint parameters. During the experiment, the sky had high elevation, light cloud cover with an global horizontal irradiance of 465 $\frac{W}{m^2}$.

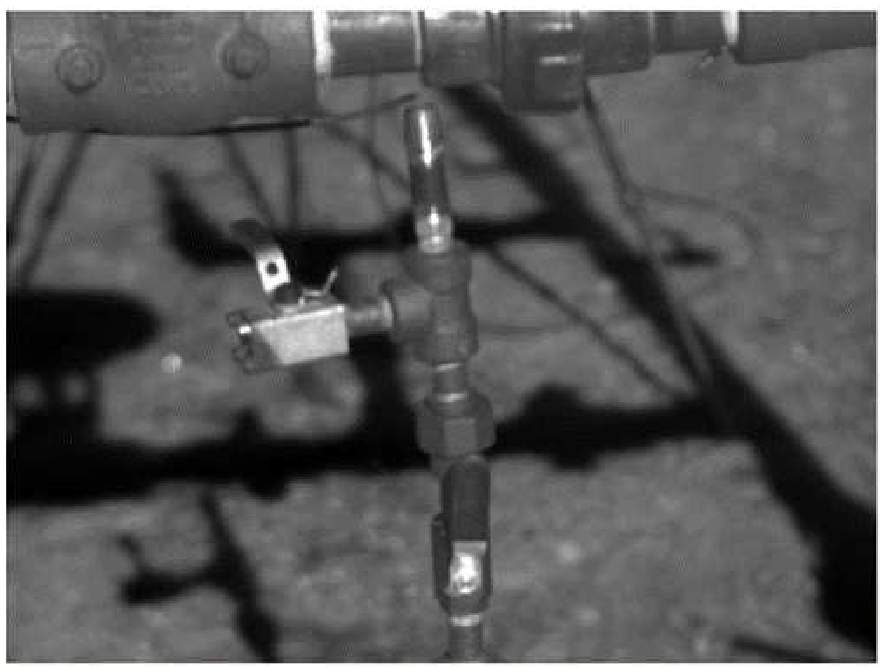

**Figure 4.3:** A frame from a recording viewing a leak rate was 96.1 g/h from a union on a well head with a viewing angle of 325 N with an imaging distance of 2 m and camera height of 1.75 m. Apparent temperature range: 9-64 °C

### 4.2.1 Application of Highpass Filter

The high pass filter removes low-frequency signal from the apparent temperature video stream. As previously discussed in Chapter 3, the frequency-based algorithm utilized a highpass filter, operator defined here as $\Xi$, with a cutoff frequency of $2.5\ Hz$, steepness of $0.85$, and stopband attenuation of $60\ dB$ [68]. The filter operates pixel-by-pixel in the $\boldsymbol{k}$ direction, as shown in Figure 4.2, and produces a filtered 3-dimensional array, $\boldsymbol{F}$.

$$F_{i,j,k} = \Xi(R_{i,j,k}) \tag{4.1}$$

The filter has a magnitude response shown in 4.4.

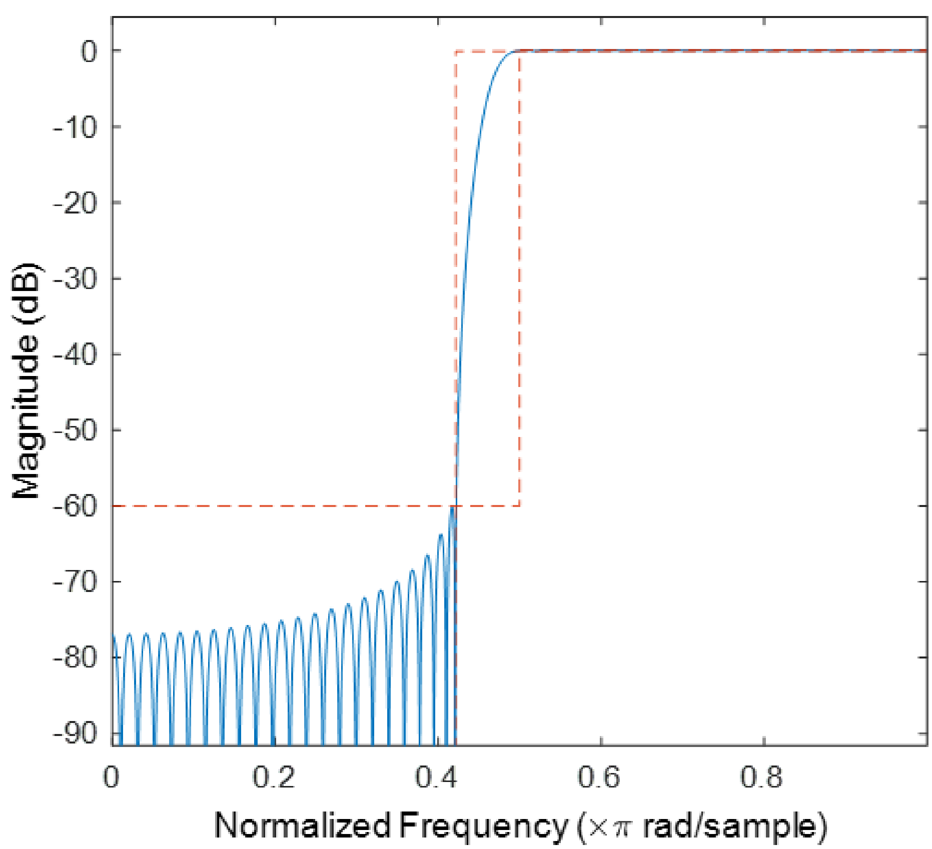


**Figure 4.4:** Plot of magnitude response curve of design high pass filter featuring a cutoff frequency of $2.5Hz$ (normalized frequency of 0.5), steepness of $0.85$, stopband attenuation of $60dB$

**Tuning Filter**

In the MATLAB® Signal Processing Toolbox™, the default values were used for steepness and stopband attenuation. The cutoff frequency was set by attempting to qualitatively optimize the signal/noise ratio. Power spectra for two pixel locations are shown in Figure 4.5, referencing pixels examined in more detail in Figure 3.7. Qualitative examination of videos from preliminary experiments indicated that grass and road pixels are representative of the span of behaviors seen in most of the videos. Examination of the power spectra indicates separation occurs between gas-on and gas-off states in the range of 2-2.5 Hz.

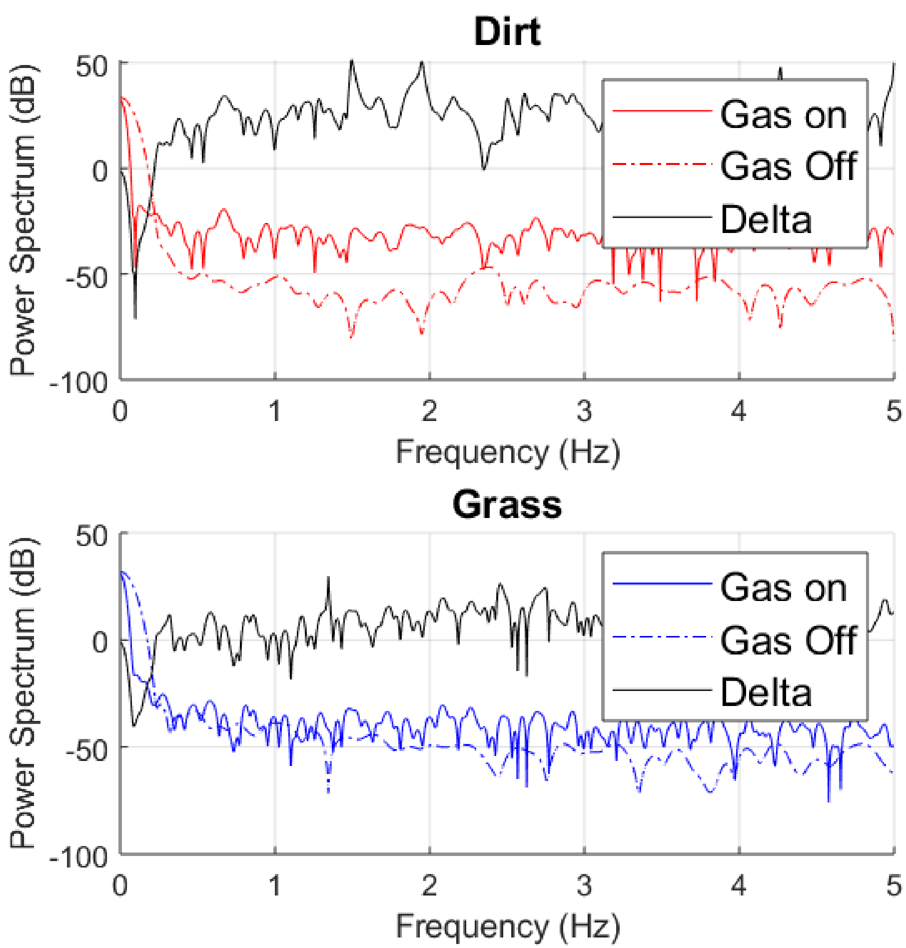


**Figure 4.5:** Power spectra of the apparent temperature signal. Delta power spectra show difference between gas on and gas apparent temperature signal. Upper plot: Power spectrum of the apparent temperature with a background of the dirt road seperated into two gas on and gas off data sets (red box in Figure 3.7). Lower plot: Similar data for a background of grass (blue box in Figure 3.7).

For the dirt plot, the power spectra separate at approximately 0.25 Hz. As for the grass plot, the power spectra diverge at frequencies >2 Hz. This is likely due to the motion of the grass as it moves in the wind, which translates into a higher frequency signal for the grass than the dirt background. The higher frequency signal caused by the plume fluctuations displays increased power above 2.5 Hz. To minimize overlap, a pass band frequency of 2.5 Hz is used.

### 4.2.2 Computing Signal Strength

Filtering the video amplified the high frequencies characteristic of the plume signal, while attenuating the low frequency drift present in all pixels. To quantify remaining signal strength, standard deviation was calculated for each pixel using the pixel values $L$ frames forward in time.

$$S_{i,j,k} = \sigma(F_{i,j,\{\kappa\}}) \ \ \{\kappa\} = k...k + L \tag{4.2}$$

where standard deviation operator, $\sigma$, is applied over the indicated data. In this work $L = 5$. This process creates a new frame where apparent temperature is replaced by the standard deviation of each pixel over $L$ frames, also in °C. At this point, the algorithm has a functional way to extract the plume signal. Figure 4.6 shows the first frame after this processing step.

**Figure 4.6:** First frame of the sample video after applying the first processing step. Gray scale displays the standard deviation array after filtering. Left panel displays the frame scaled to full range ($2.8 \times 10^{-3}$ to 2.9 °C) while right panel is clipped to enhance the plume visibility ($2.8 \times 10^{-3}$ to 0.5 °C).

### 4.2.3 Data Spikes and Noise

After the previous step, the algorithm has enhanced any pixels which contain substantial frame-to-frame variation, i.e. movement. The frequency-based algorithm identifies the plume by its fluctuations due to the wind, and objects in the background which are moving similarly (e.g. a flag or tag flapping in the wind) will exhibit similar high frequency signals. These locations may be identified as part of a gas plume, exaggerating the fraction of the scene containing visible gas plume movement. Similarly, areas with neither gas plume nor extraneous motion are still subjected to random, high frequency, noise in the apparent temperature, due to apparent temperature noise in the camera system or random atmospheric variations between the object and the camera. The magnitude of this noise signal is shown in Figure 3.8 and 3.9, and is typically $\leq$5% of $\boldsymbol{S}$ for pixels in the gas plume. This algorithmic step eliminates – zeros out – pixels with these characteristics.

Investigation indicated that gas plumes exhibit a unique, continuous Gaussian shape in the $\boldsymbol{i}$ and $\boldsymbol{j}$ directions. To filter out items dissimilar to this typical shape, a 2D filtering method is utilized [69]. This method considers each frame, $S_k$, of $\boldsymbol{S}$, and applies Gaussian 'blur' filter, $\mathcal{G}$, with $\sigma_f = 10$ and a filter size of 15, which creates a "blurring effect" on each frame, smoothing large data spikes [69]. Undesired signals can be identified by looking at the absolute difference between the filtered and unfiltered signal strength arrays, defined in Equation 4.3:

$$\boldsymbol{\Delta} = |\mathcal{G}(\boldsymbol{S}) - \boldsymbol{S}| \tag{4.3}$$

where $\mathcal{G}(\boldsymbol{S})$ is $\boldsymbol{S}$ after applying the Gaussian filter.

We then apply two rules. First, if $\Delta_{i,j,k} > \delta_s$, that pixel is identified as movement other than a gas plume (i.e. a data spike) and is set to zero. Second, the apparent temperature noise signal is eliminated by setting all pixels in $\boldsymbol{S}$ to zero if $S_{i,j,k} < \delta_n$. For this study $\delta_s = 0.1$ and $\delta_n = 0.05$. A sensitivity study to select these values is discussed below.

$$\hat{S}_{i,j,k} = \left\{ \begin{array}{rl} 0 & : S_{i,j,k} < \delta_n \\ S_{i,j,k} & : \delta_n \leq \Delta_{i,j,k} \leq \delta_s \\ 0 & : \Delta_{i,j,k} > \delta_s \end{array} \right\} \tag{4.4}$$

Figure 4.7 visually shows the effect of Equation 4.4.

**Figure 4.7:** Standard deviation array showing the effect of eliminating data spikes and noise floor. Data plotted on a full scale. Temp range: 0 – 0.34 °C

### Data Spike Tuning

Stationary objects moving in the wind are typically constrained to a small number of pixels in the field of view. This constrains motion to a small number of pixels and amplifies the values of $\boldsymbol{S}$ for those pixels relative to other nearby pixels. These constrained, large, motions appear as bright (i.e. high value) spots in $\boldsymbol{S}$ with sharp edges – the equivalent of a bright spot on a photograph caused by a specular reflection. For the first frame of one preliminary recording, the calculated $\boldsymbol{S}$ value is shown as a surface plot in Figure 4.8. The large data spike is from a tag flapping in the background of the video image.

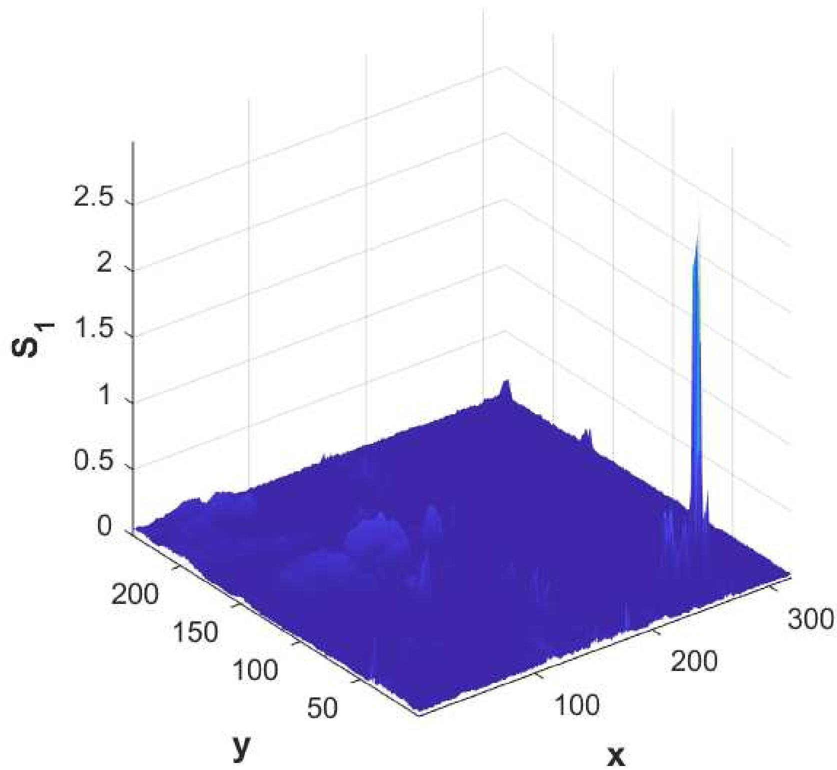


**Figure 4.8:** Raw $S_k$ plot showing data spike from a waving tag

A Gaussian "blur" filter is a commonly utilized image processing method that smooths high-contrast regions of an image. For this study, edges were filtered using a Gaussian filter, $\mathcal{G}$, with $\sigma_f = 10$ and a filter size of 15. Filter parameters were developed by trial and error, and are effectively set by the expected size of moving objects in the background. Similar filter parameters should work in a wide range of conditions; if objects are much larger, their motion will interfere with the plume visibility, and if much smaller, the motion will have minimal impact on the image.

The filter is applied to each frame, $S_k$, of $\boldsymbol{S}$. This filter applied to Figure 4.8 is shown in Figure 4.9.

Undesired signals can be identified by looking at the absolute difference between the filtered and unfiltered signal strength arrays, defined as $\boldsymbol{\Delta} = |\mathcal{G}(\boldsymbol{S}) - \boldsymbol{S}|$, where $\mathcal{G}(\boldsymbol{S})$ is $\boldsymbol{S}$ after applying the Gaussian filter.

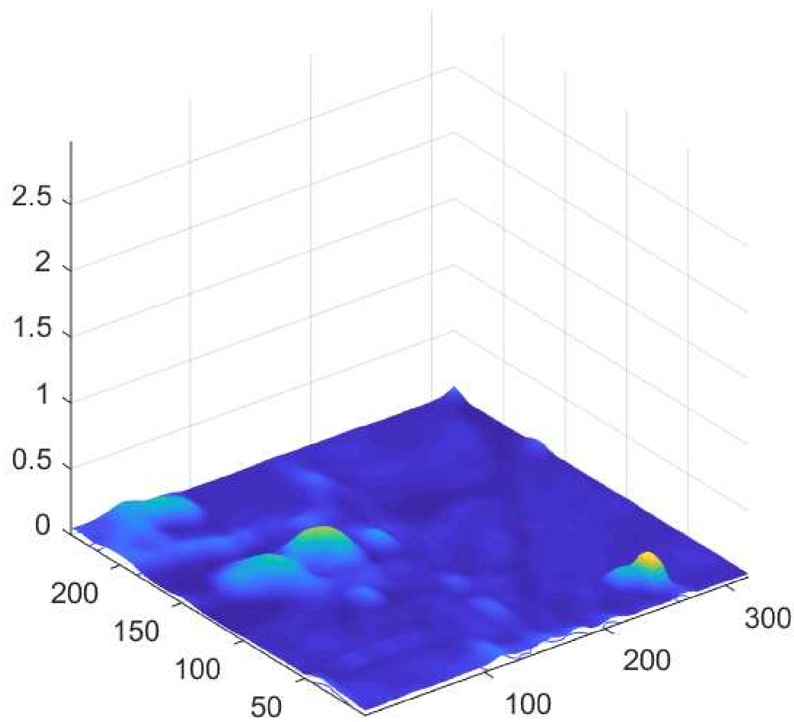


**Figure 4.9:** Gaussian blur filter applied to Figure 4.8. $\Delta_{i,j,k}$, used in Equation 4.4, is defined as the difference is pixel value between Figure 4.8 and this surface plot.

If $\Delta_{i,j,k} > \delta_s$, that pixel is identified as movement other than a gas plume (i.e. a data spike) and is set to zero. The values of $\delta_s = 0.05, 0.1, 0.2$ were tested, and are shown in the next three figures:

- Figure 4.10: $\delta_s = 0.05$. The required change in pixel value from the gaussian blur results in plume signal being interpreted as a spike and portions of the plume are is zeroed out.
- Figure 4.11: $\delta_s = 0.2$, the required change in pixel value is too large. This leaves too much of the data spike unfiltered.
- Figure 4.12: $\delta_s = 0.1$ results in a the "just right" region where plume signal is not filtered, but the data spike filtering is still maximized.

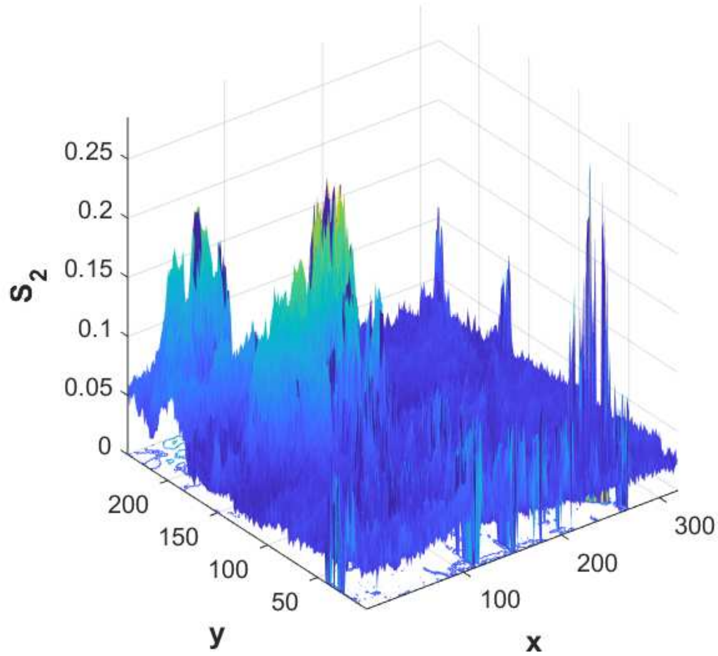


**Figure 4.10:** $\delta_s = 0.05$. When $\Delta_{i,j,k} > \delta_s$ is true, the pixel value is zeroed. Some plume signal is zeroed.

#### Noise Tuning

The cumulative probability function (CDF) plot in Figure 4.12 demonstrates the transition from absence of plume information to the presence of a plume. By setting a threshold value so the top 15% of the array values are transmitting plume information, the resultant $\boldsymbol{S}_b$ value of $\delta_n = 0.05$ presents itself.

### 4.2.4 Shimmer Effect

Up until this point, the algorithm functioned with no knowledge of whether the gas emission is present or not. Natural gas equipment often contains piping and components that are cylindrical. In bright sunlight, the cylindrical surface areas roughly tangential to the direction of view tend to *shimmer*, due to random, high-frequency variations in reflected, direct normal irradiance, camera vibration or other factors. The shimmering edges tend to outline piping and components as seen in Figure 4.7. To eliminate these artifacts, the algorithm utilizes frames taken during the gas-off time to eliminate shimmering pixels from detected plumes. Note that prior algorithm steps process the

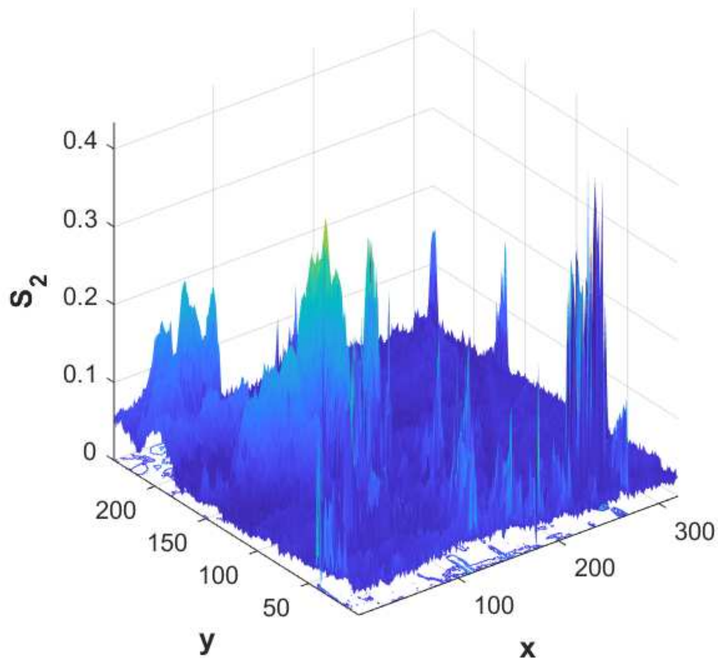


**Figure 4.11:** $\delta_s = 0.2$. When $\Delta_{i,j,k} > \delta_s$ is true, the pixel value is zeroed. Data spike signal is still prominent

entire video stream, while this step separates $\hat{\boldsymbol{S}}$ into two sequences, before ($\hat{\boldsymbol{S}}_b = \hat{S}_{i,j,k=1...k_t}$) and after ($\hat{\boldsymbol{S}}_a = \hat{S}_{i,j,k=k_t...N}$) gas stopped flowing.

To remove shimmer, a pixel weight is developed by identifying all pixels that exceeds the noise threshold,

$$I_{i,j,k} = \begin{Bmatrix} 1 & : \hat{S}_{i,j,k} > \delta_n \\ 0 & : \hat{S}_{i,j,k} \leq \delta_n \end{Bmatrix} for\ k = 1...N \tag{4.5}$$

and then computing $\bar{\boldsymbol{I}}$, the mean of $\boldsymbol{I}$ in the $\boldsymbol{k}$ direction in the gas off state ($k = k_t..N$), on a per-pixel basis, and constructing a weighting matrix, $\boldsymbol{W}$ where:

$$W_{i,j,k} = (1 - \bar{I}_{i,j}) \cdot I_{i,j,k} \ \ for\ k = 1...N \tag{4.6}$$

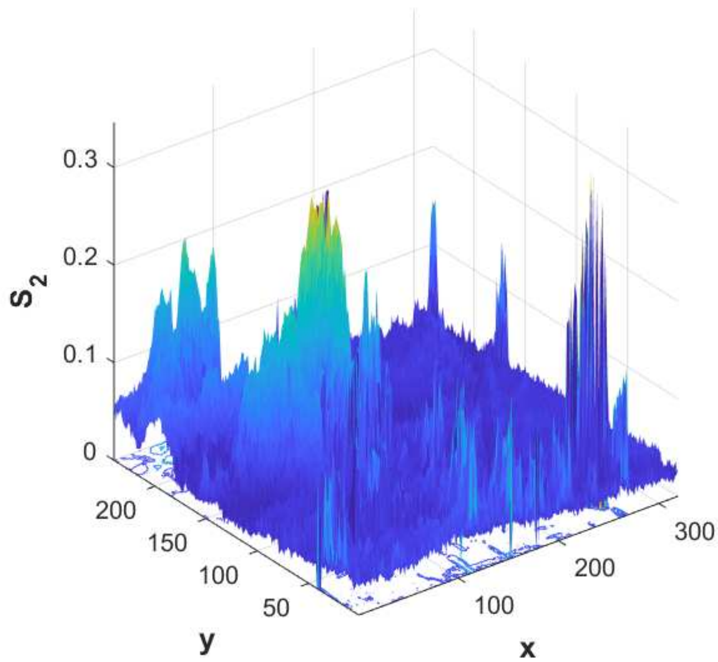


**Figure 4.12:** $\delta_s = 0.1$. When $\Delta_{i,j,k} > \delta_s$ is true, the pixel value is zeroed. "Just right" value between $\delta_s = 0.05$ and $\delta_s = 0.2$

Pixels with the shimmer effect are identified as $D_{i,j,k} > \delta_c$ and eliminated from the identified gas plume. For this study $\delta_c = 0.95$. A sensitivity study was completed to select these values. Applying this test:

$$D_{i,j,k} = \left\{ \begin{array}{ll} 1 & : W_{i,j,k} > \delta_c \\ 0 & : W_{i,j,k} \leq \delta_c \end{array} \right\} for\ k = 1...N \tag{4.7}$$

**Shimmer Tuning**

A range of $\delta_c$ values were qualitatively tested. Figure 4.14 shows a series of frames from a typical recording, with $\delta_c = 0.1, 0.5, 0.7, 0.9, 0.95, 0.99$ shown in the upper left, upper middle, upper right, lower left, lower middle, and lower right positions, respectively. Focusing on the piping above the emission, the shimmer effect is minimized as $\delta_c$ approaches a value of 1. However, as this is happening, the value increases the likelihood of inadvertently eliminating plume signal. To approximately maximize plume signal while minimizing the shimmer effect, $\delta_c = 0.95$.

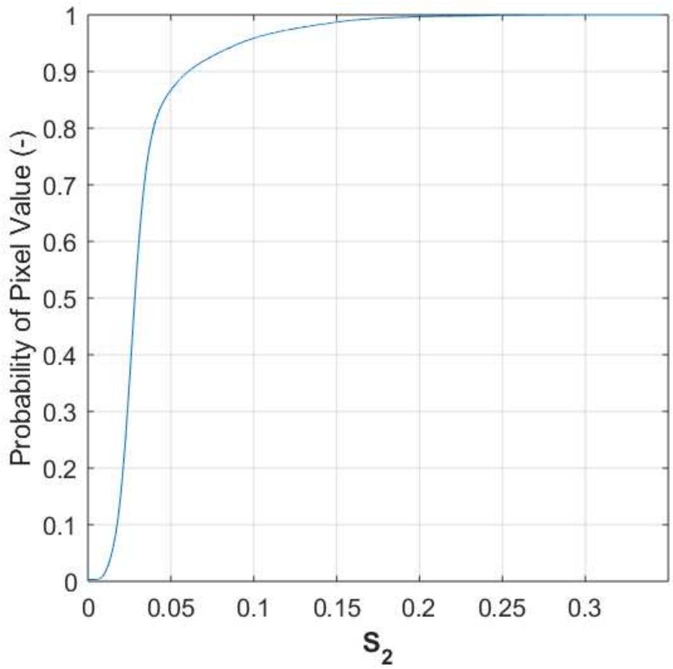


**Figure 4.13:** Noise threshold tuning. The plot shows the cumulative probability function of all pixel values in $\boldsymbol{S}$ after application of the Gaussian blur filter. Higher values of $S_{i,j,k}$ indicate higher signal strength indicative of the presence of a plume. Lower signal values indicate background.

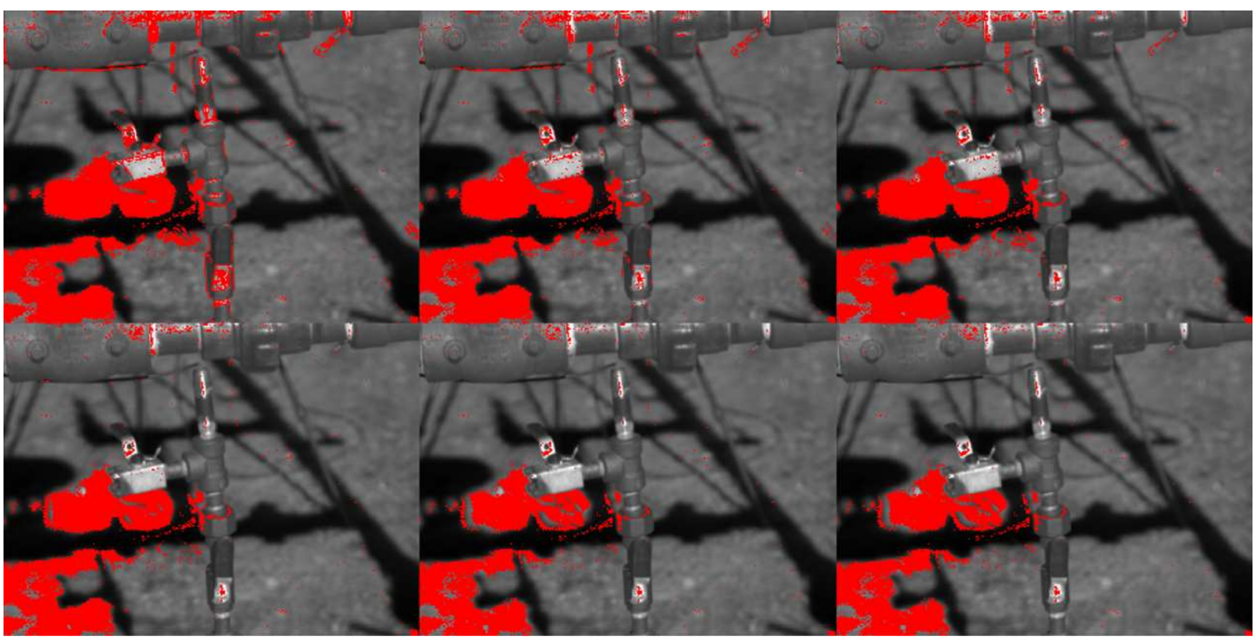

**Figure 4.14:** Shimmer elimination plot of various $\delta_c$. $\delta_c = 0.1, 0.5, 0.7, 0.9, 0.95, 0.99$ shown in the upper left, upper middle, upper right, lower left, lower middle, and lower right positions, respectively. Temp range: 9 to 64 °C

### 4.2.5 Plume Coverage Fraction

$\boldsymbol{D}$ contains ones where a gas plume is detected. Plume size in each gas-on frame is computed by calculating the number of plume pixels in each frame relative to the total number of pixels (240x320). The result is a vector of plume coverage fractions, $C_k, k = 1...k_t$, representing the fraction of each frame area where the gas plume is visible in each frame. This is represented in equation 4.8 with $nnz$ as a function to count the number of 1 values in the frames, and $\tau$ as the total pixel count (for a 240 x 320 matrix, $\tau$ = 76800).

$$C_k = \frac{nnz(D_{i,j,k})}{\tau} * 100 \;\; for\; k = 1...N \tag{4.8}$$

For the gas-on frames, we can now create a histogram and calculate the mean, median and standard deviation of this data set. The mean of $C_k$ is representative of the the average fraction of the FOV where the plume is visible. This metric will hereafter be referred to as "PCF".

# Chapter 5

# Low Flow Experiment

## 5.1 Background Motivation

This chapter discusses the experiments conducted to demonstrate the potential applications of the developed plume extraction algorithm. A previous study took an experimental approach to analyze the effect of imaging distance (1.5, 3, 6 m) and emission rate (0, 3.5, 8.9, 17.7, 26.6, 35.4, 71, 177 g/h) had on the operator's ability in emission detection to develop probability curves on the likelihood of detection [36]. This operator was trained in methane emission detection and has obtained his OGI certification from Infrared Training Center located in Dallas, Texas. It was found that when using a FLIR™ GF320 handheld OGI camera the median detection limit, or 50% likelihood of detection was approximately 20 g $CH_4$/h at an imaging distance of 6 m [36] while surveying in high sensitivity mode [37].

## 5.2 Imaging Distance and Viewing Angle vs Emission Rate

Results from the GTD preliminary experiments indicated that frequency analysis of video frames provides a robust metric that identifies areas of the FOV which contain a gas plume. To assess the impact of emission rate, viewing angle, and imaging distance on emission visibility, two separate but similarly structured experiments were conducted. These tests utilized emissions in pseudo-realistic conditions – a well head at the METEC site. Viewing angle experiment was designed to emulate a camera operator imaging a single component from multiple viewing angles. Imaging distance experiment was designed to emulate a camera operator imaging a single component from multiple imaging distances.

The experimental plan is illustrated in Figure 5.1.

| Imaging Distance [m] / View Angle [deg] / Camera Number | DOE 2 | DOE 1 | 5 | | | | | | | |
|---|---|---|---|---|---|---|---|---|---|---|
| | (a) 6 | (b) 32 | | | | | | | | |
| | 5 | 75 | 4 | | | | | | (c) | |
| | 4 | 145 | 3 | | | | | | | |
| | 3 | 202 | 2 | | | | | | | |
| | 2 | 268 | 1 | | | | | | | |
| | 1 | 325 | 0 | | | | | | | |
| **Leak Rate [g/h]** | | | | 17 | 43 | 71 | 96 | 119 | 142 | 165 |
| Recording Set ID | | | | 1 | 2 | 3 | 4 | 5 | 6 | 7 (d) |
| | | | | 8 | 9 | 10 | 11 | 12 | 13 | 14 |
| | | | | 15 | 16 | 17 | 18 | 19 | 20 | 21 |

**Figure 5.1:** Overall framework of DOE1 and DOE2 featuring (a) Camera imaging distances (b) Cardinal angles each camera is looking to view the emission (c) Each empty box representing a recording with the respective set of independent variables (d) Emission rates repeated in recording sets 8-21 to increase data collection.

The experiment controls three variables:

- *Viewing Angle:* To emulate a camera operator viewing a single component from multiple viewing angles. Six cameras are positioned equidistant around the emission with approximately evenly spaced viewing angles.

- *Imaging Distance:* To emulate a camera operator imaging a single component from multiple imaging distances. Six cameras are positioned with similar viewing angles with increasingly larger imaging distances.

- *Emission rate:* Emission rate is controlled by a combination of pressure regulators and three solenoid valve orifices to allow for 8 varying emission rates. For each experiment, gas is released at various emission rates (17-196 g/h) for a gas-on phase directly followed by a gas-off phase.

Wind speeds and ambient temperatures were not controlled. Weather conditions throughout viewing angle and imaging distance experiments are discussed in the following sections. Conditions for each viewing angle and imaging distance experiments are in *DataMaster.xlsx*, sheet *ViewingAngle vs LeakRate* and *ImagingDistance vs LeakRate*, respectively.

Viewing angle and imaging distance experiments consist of 21 recording sets. Recordings 8-21 are repeated to increase data collection.

## 5.3 Experimental Setup

### 5.3.1 Viewing Angle Experiment

The six cameras were arranged around an emission location, spaced approximately 60 degrees apart, as shown in Figure 5.2. The gas release point is a pipe union 87 cm from the ground. Cameras were mounted on tripods such that the lens center of the camera body was approximately 1.75 m from the ground. In this configuration, the background of the well pad equipment was the ground (gravel aggregate) for all cameras. All recordings were completed in the the early afternoon of November 14th, 2019. The ambient temperature was 10.2 to 11.3 °C and wind speed 1.9 to 3.1 m/s. Wind bearing varied from 117°N (from camera 4 toward camera 1) to 166°N (from camera 5 toward camera 2). During the viewing angle experiment, the sky had high elevation, light cloud cover with an irradiance of 420 to 477 $\frac{W}{m^2}$. All weather condition data throughout experiment is found in *DataMaster.xlsx* sheet *ViewingAngle vs LeakRate*.

On/off valves in series with precision orifices were used to achieve the 7 emission rates of 17, 43, 71, 96, 119, 142, and 165 g/h. Flow rates were measured using thermal mass flow. Table 5.1 shows the released market gas composition.

The emission rates were repeated in recording sets 8-21 to increase data collection. All recordings sets were completed in the early afternoon with total experimentation time spanning 43 minutes, resulting in consistent wind speeds and directions.

One sample data set of processed recordings from all cameras for an emission rate of 96 g/h can be found in *SupplementalData.zip*.

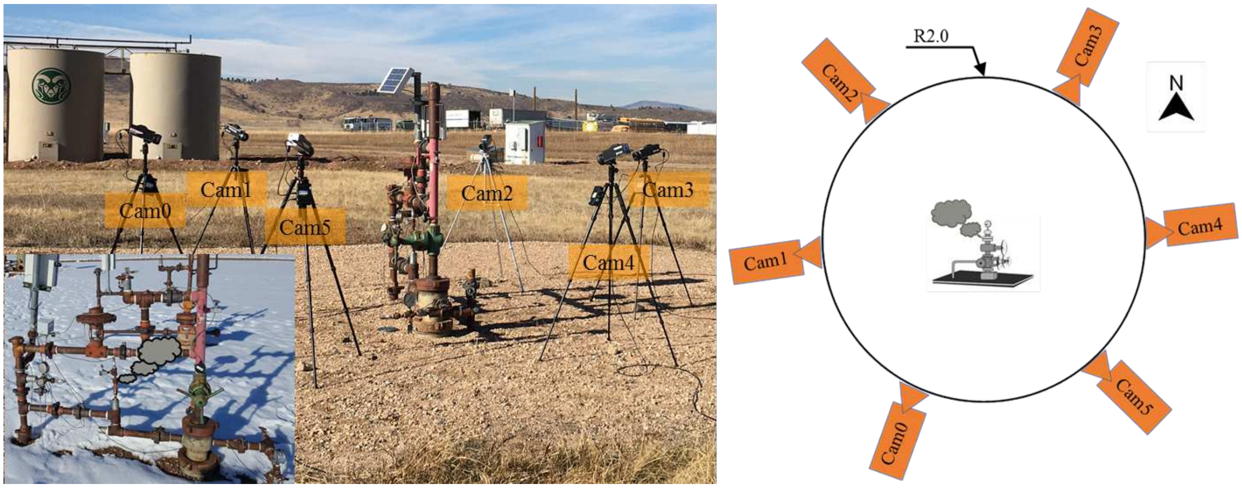


**Figure 5.2:** Left Figure: Viewing angle experimental setup of six cameras surrounding a well head emission point. Emission point is shown in inset photograph, taken at after the experiment. Right Figure: Birds eye view of surrounding cameras. All camera viewing angles found in *DataMaster.xlsx* sheet *AllExperiment-MetaData*

**Table 5.1:** Released market natural gas composition

| Molecule | Mole Fraction | Mole Fraction $\sigma$ |
|---|---|---|
| $N_2$ | 0.00550 | 3.28E-05 |
| $CO_2$ | 0.01877 | 7.04E-05 |
| C1 | 0.85750 | 0.000517 |
| C2 | 0.10295 | 0.000390 |
| C3 | 0.01276 | 4.79E-05 |
| iC4 | 0.00080 | 6.15E-06 |
| nC4 | 0.00156 | 5.24E-06 |
| iC5 | 0 | 0.00E+00 |
| nC5 | 0 | 0.00E+00 |
| C6 | 0.00013 | 1.02E-05 |

### 5.3.2 Imaging Distance Experiment

The imaging distance experiment holds the viewing angle roughly constant and varies the distance from the camera to the emission. This simulates a camera operator viewing the same component from multiple distances, at a range of emission rates. The six cameras were positioned as shown in Figure 5.3. All cameras viewed the emission from approximately the same viewing angle as camera 0 in the viewing angle experiment (35° N). The viewing angle was offset slightly to provide an imaging distance for cameras 0-5 of 1, 2, 3, 4, 5, and 6 m, respectively. Similar gas release rates were utilized for this imaging distance experiment as for the viewing angle experiment, and each release rate was repeated three times. All recordings were completed the late-afternoon of January 28th, 2020. The ambient temperature was 5.1 to 7.3 °C, and wind speed 1.8 to 3.0 m/s. Wind bearing varied from 138° N to 187° N (approximately from behind and towards the left for all cameras' FOV). During the imaging distance experiment, the sky had high elevation, light cloud cover (see Figure 5.3) with an irradiance of 12.9 to 151.8 $\frac{W}{m^2}$. All experiment data and weather conditions can be found in *DataMaster.xlsx* sheet *ImagingDistance vs LeakRate*.

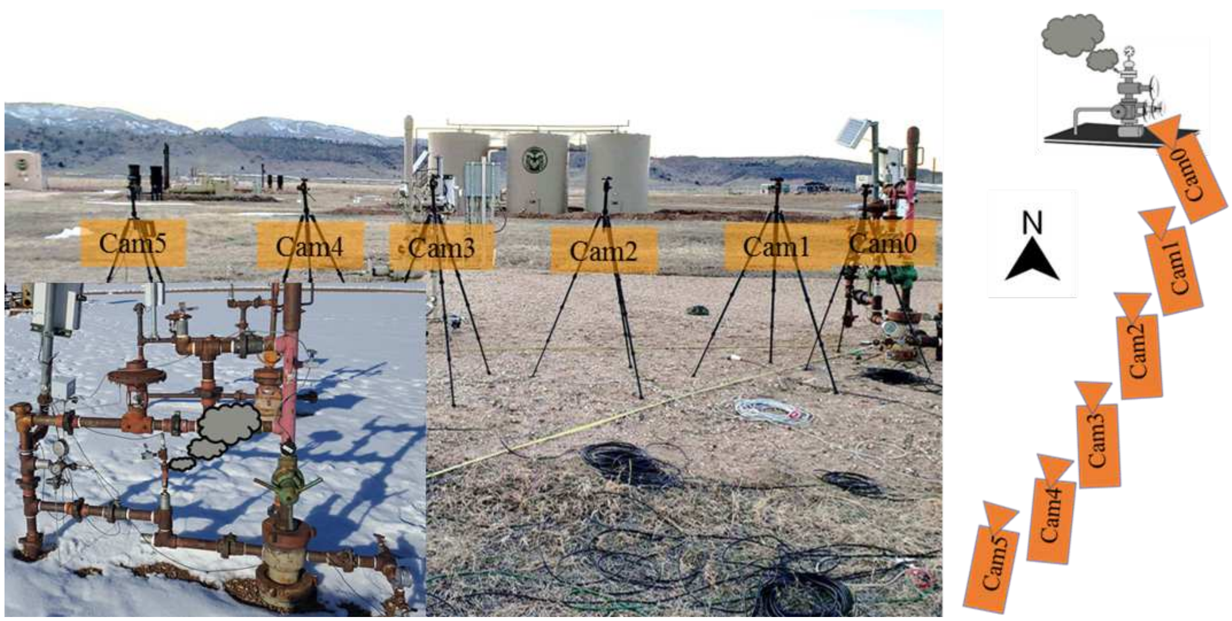


**Figure 5.3:** Left figure: Imaging distance experimental setup of six cameras surrounding a well head emission point with well head emission point inset. Right figure: Birds eye view of surrounding cameras. All camera viewing angles found in *DataMaster.xlsx* sheet *AllExperimentMetaData*

The manifold pressure setting of the source gas supply was slightly higher than the viewing angle experiment, resulting in the emissions rates of 21, 53, 86, 113, 142, 169, and 196 g/h. All emission rates were repeated two additional times. All experiments were completed in 44 minutes, resulting in consistent wind speeds and directions. Table 5.1 shows the released gas composition.

One sample data set of processed recordings from all cameras for an emission rate of 113 g/h can be found in *SupplementalData.zip*.

## 5.4 Testing Environment Background

All experiments for this work were conducted at METEC in Fort Collins, Colorado. As previously discussed in Chapter 2, METEC simulates natural gas emissions as they may occur in the field to test/train/qualify operators in various emission detection methods. To control emission rates from equipment, METEC uses on/off solenoid valves in series with choked flow orifices to control flow rates. Actual flow is then measured near the gas supply. This section will discuss the background of the mass flow controller, valve configurations, and the user interface used to control the site.

### 5.4.1 Emission Rate Measurement

Natural gas at METEC is supplied using compressed gas stored at approximately 2500 psi, which is regulated down to a low manifold pressure of 10-100 psi before being routed to the release point. Gas is released through choked flow orifices using on/off control valves to control which orifices are active. The combination of manifold pressure and valve state sets the flow rate of the emission point.

Emissions are measured using a thermal mass flow meter, an Aalborg (Model Number: GFC17A-VAL6-A0) calibrated on pure methane composition. The meter has an upper flow limit of 15 standard cubic feet per hour and has an accuracy of 1% of the full scale, or 0.015 SCFH (3.26 g/hr). Additional error is expected as the MFC was calibrated with pure methane. For a flow rate conversion calculator see *DataMaster.xlsx* sheet *FlowrateConverter*.

All weather conditions 5 minute average data including temperature, wind speed, wind bearing, and irradiance were obtained from the Christman weather station located about 100 m from the experiment site. Weather data was matched with time stamps $\pm$ 2.5 minutes with respect to obtained data. All timestamps and weather condition data is paired with PCF value in *DataMaster.xlsx*, sheets *ViewingAngle vs LeakRate* and *ImagingDistance vs LeakRate*.

# Chapter 6

# Algorithm Validation and Experimental Results

Chapter 4, Algorithm Methodology, discussed the algorithm that processes OGI recordings to develop the PCF metric. To demonstrate application of the algorithm, the viewing angle and imaging distance experiments were conducted and was the topic of Chapter 5, Low Flow Experiment. This chapter discusses how the algorithm was validated, the processed results from the viewing angle and imaging distance experiments, and the relationship between the PCF metric and human *probability of detection*.

## 6.1 Validation of Algorithm to Replicate Expert Abilities

For the PCF metric to be a useful indicator of the probability of detection for human operators, the method must be compared to human review of similar OGI videos. To accomplish this, the study had 5 OGI experts evaluate some recordings captured during the viewing angle experiment and indicate whether a plume was or was not visible.

A 28-question evaluation was created consisting of a 10 s snippet of each flow rate recording from three of the six camera view points with an imaging distance of 2 m. Seven recordings with the gas off were added to act as a control. Table 6.1 summarizes the evaluation. In practice, 10 seconds is on the upper end of the length of time an operator views each component during and OGI screen, and thus provides a higher probability-of-detection than would likely occur in routine field conditions.

**Table 6.1:** Summary of expert evaluation to compare algorithm results to Y/N emission identification

| Camera | Emission Rates [g/h] | # of Questions |
|---|---|---|
| 0 | 16, 41, 68, 92, 115, 137, and 158 | 7 |
| 2 | 16, 41, 68, 92, 115, 137, and 158 | 7 |
| 4 | 16, 41, 68, 92, 115, 137, and 158 | 7 |
| Control | 0 | 7 |

In this data set, recordings were completed in the the early afternoon of November 14th, 2019. The ambient temperature was 10.1 to 10.8°C and wind speed 1.9 to 2.8 m/s. Wind bearing varied from 121° N (from camera 4 toward camera 1 ) to 166° N (from camera 5 toward camera 2). During the viewing angle experiment, the sky had high elevation, light cloud cover with an irradiance of 459 to 477 $\frac{W}{m^2}$. Evaluation data set experimentation time lasted 13 minutes.

Evaluation questions were in a randomized order. The five OGI experts were allowed to watch the 10 s snippet recordings one time then immediately report on a yes/no (Y/N) basis if the they could see an emission. Evaluation data can be accessed in *DataMaster.xlsx* sheet *ExpertEvalLogReg*.

## 6.2 Probability of Emission Detection

To pair the results of this evaluation to the mean value of the $C_k$ vector, PCF, a logistic regression was created. The regression shown in Figure 6.1 reports the likelihood an expert will identify an emission with respect to the developed PCF metric.

The median and 90% probability of detection correlates to the plume covering 6.8% and 13.8% of the cameras field of view, respectively. Due to potential false positives, there is 11% chance of detection when the gas is off.

**Table 6.2:** Summary of logistic regression results showing the probability of detection for various plume coverage fraction values.

| Plume Coverage Fraction | Probability of Detection [%] |
|---|---|
| 0.00 | 10.59 |
| 3.3 | 25 |
| 6.8 | 50 |
| 13.8 | 90 |
| 16.2 | 95 |
| 21.5 | 99 |
| Inf | 100 |

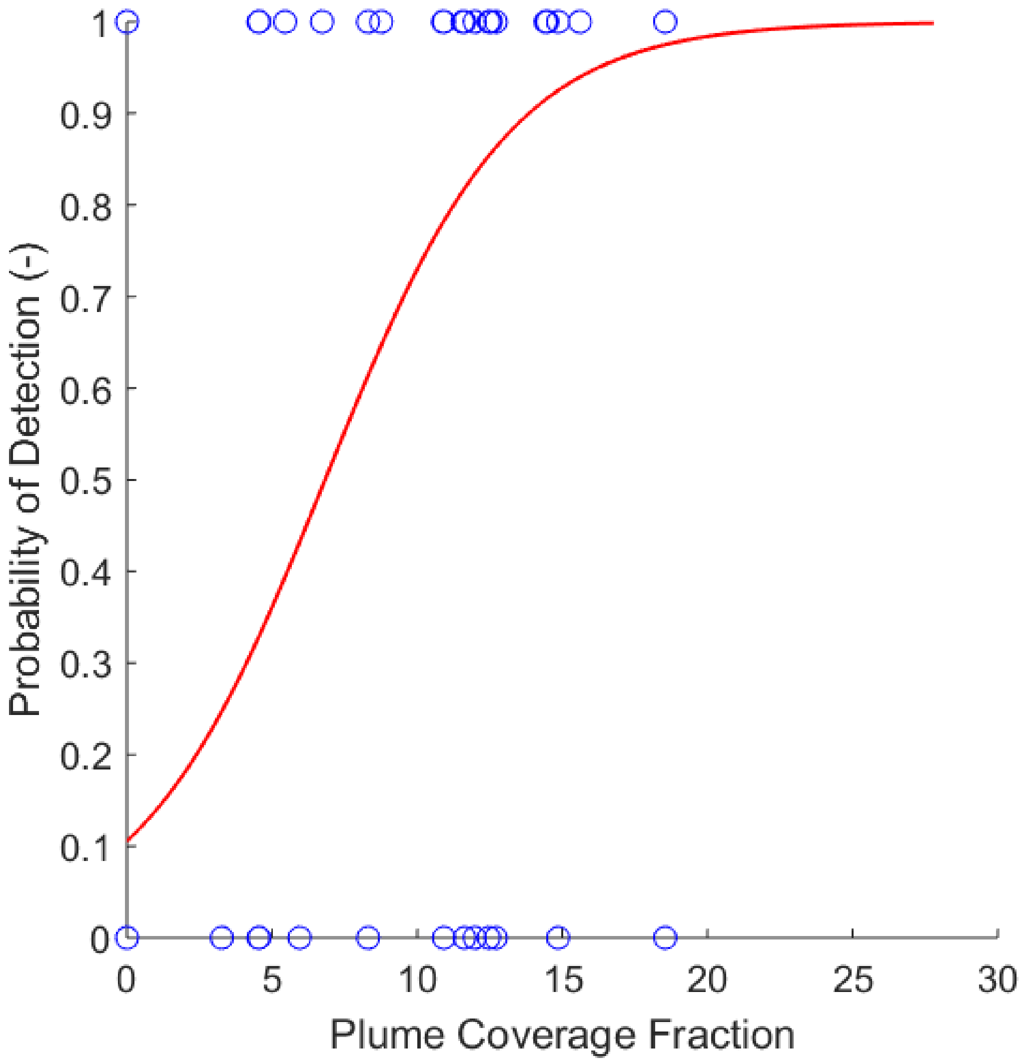


**Figure 6.1:** A logistic regression showing the probability of detection with respect to the PCF metric. Logistic regression parameters are $\beta_1$ = -2.13, $\beta_2$ = 0.313. Table 6.2 provides results of the regression for a range of PCF values.

Results of the logistic regression indicate a relationship between the probability of detection and PCF, indicating that the PCF metric could be used to understand the detectability of plumes without human evaluation.

## 6.3 Experimental Results

To demonstrate the potential application of the algorithm, the viewing angle and imaging distance experiments were conducted, recordings were processed, and experimental data was analyzed.

### 6.3.1 Viewing Angle Experiment

The viewing angle experiment discussed in Section 5.2 consisted of 21 recording sets, with six cameras creating 126 PCF data points with respect to emission rate and viewing angle. A camera recording error for camera 0 at an emission rate of 71.5 g/h caused the camera feed to briefly disconnect mid-recording. Therefore the third data point was removed from the data set.

Examination of the data indicated a linear relationship between emission rate and PCF. An example is shown in Figure 6.2 for a viewing angle of 32° N (camera 0). The figure overlays the PCF data and a linear regression. For this viewing angle and with an imaging distance of 2 m, a linear trend line is shown with a y-intercept value of $y_0 = 0$, a slope m = 9.4E-2, and a R-squared value $R^2 = 0.789$. Similar analysis of all other cameras show similar data trends.

For all viewing angles (cameras 0-5), the mean and range of the three emission rate data points was calculated and shown in Figure 6.3. Emission rate error was calculated as 1% of the MFM's full range, or ±3.26 g/h.

There is a relatively strong linear relationship between the PCF and the emission rate regardless of viewing angle, suggesting that the point of view of which camera operator is viewing an emission relative to the wind bearing is less significant than emission rate.

### 6.3.2 Imaging Distance Experiment

The imaging distance experiment discussed in Section 5.2 consisted of 21 recording sets, with six cameras recording creating 126 PCF data points with respect to emission rate and imaging distance. For all imaging distances, the range and mean PCF values were calculated for each

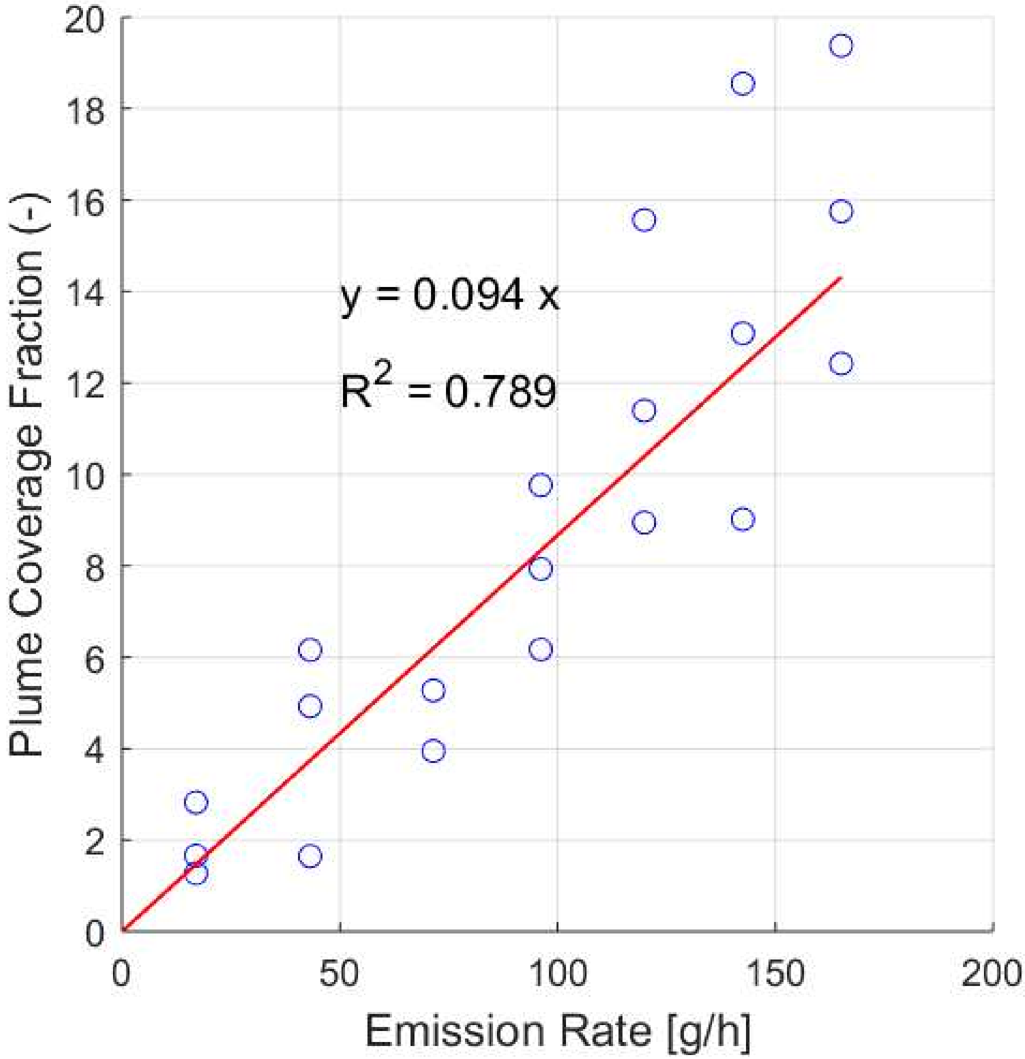


**Figure 6.2:** Linear relationship between PCF and Emission Rate for camera 0 at 2 m with $R^2 = 0.789$ and slope, m = 9.4E-2

emission rate, as with the previous experiment, the emission rate error was set to 1% of the MFM's full range, or $\pm$3.26 g/h. The mean, range, and emission rate error are shown in Figure 6.4

Similarly to varying viewing angle and emission rate at a 2 m viewing distance, imaging distances of 1 and 2 m also show a linear relationship between PCF and emission rate. However, at distances greater than 2 m, PCF does not increase with emission rates, indicating that emission identification is unlikely. Since the image of an object decreases in size with the square of the distance, the drop off in PCF – a measure of plume size – is unsurprising. This analysis indicates

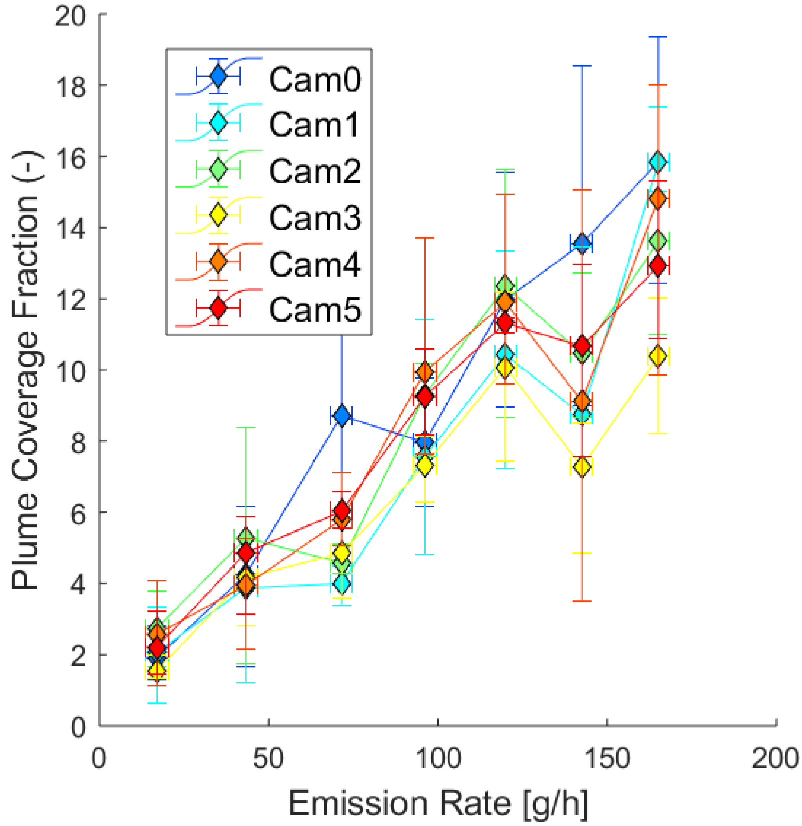


**Figure 6.3:** Similar relationship between PCF and emission rate for all viewing angles/cameras. Emission rate error for all points is $\pm$ the full range of the MFM ($\pm$3.26 g/h). PCF bars show the minimum and maximum values with points at the average PCF of the three trials.

that, for these leak rates, distances, and weather conditions, the noise floor for PCF is between 1% and 2% of the FOV.

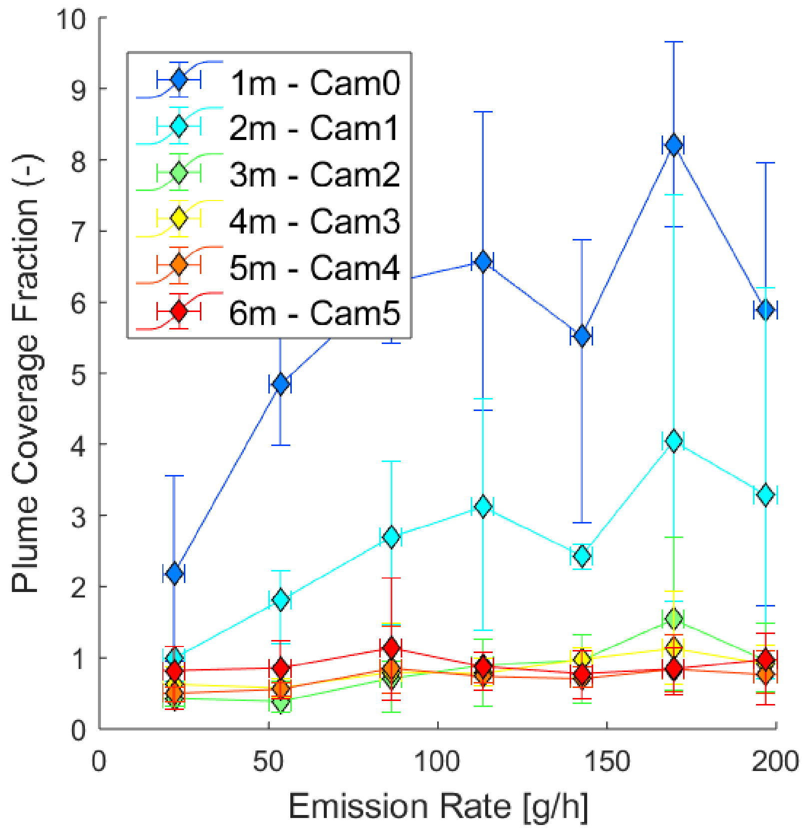


**Figure 6.4:** Impact of imaging distance on the plume coverage fraction. Emission rate error for all points is ± the full range of the MFM (±3.26 g/h). Plume coverage fraction bars show the minimum and maximum values with respect to the average of the three recordings. Decrease in PCF relative to viewing angle experiment is likely due gas passing behind a pipe.

# Chapter 7

# Conclusions and Future Work

This novel frequency-based algorithm provides a method to experimentally analyze the effect independent variables have on the plume coverage fraction and visibility of a natural gas emission plume. This method requires time-series of apparent temperature data for each pixel in an OGI camera recording, recorded by a stationary camera in both gas-on and gas-off states.

The development of a quantitative post-processing algorithm provides an automated means to assess the detectability of emission plumes without relying on human interpretation of OGI videos. Preliminary experimentation revealed that natural gas emissions contain high-frequency signal. Analysis showed these signal can be isolated from background through a series of processing steps. The developed frequency-based algorithm proposed here allows for pixel independent analysis of transmitted plume signal through apparent temperature data to output a metric representing the new measure of detectability (PCF). Through OGI expert validation and evaluation, a logistic regression reported how the probability of detection increases with respect to the PCF. An analysis was completed on how this plume signal varies with viewing angle, imaging distance, and emission rate. A linear relationship was found between emission rate and the PCF at a tested imaging distance of 2 m. The viewing angle effect on PCF for all cameras at an imaging distance of 2 m resulted in almost no noticeable effect. Imaging distance has a power-low relationship the PCF and therefore the likelihood of positive emission detection.

## 7.1 Future Work

This study revealed a promising novel frequency-based algorithm for separating natural gas emission movements from the stationary background and laid the ground work for subsequent OGI research based studies. Although effective, there is room for growth and improvement of the algorithms techniques and applications. Foremost, additional tuning of threshold values could increase the effectiveness of the algorithm in specific background scenarios. Partnering with similar researchers to determine effectiveness should be pursued. Validation to other machine vision or deep learning computational methods to quantitatively compare the error associated between similar methods should be conducted.

This method has the potential to ground previous work that utilized the opinion of camera operators to determine OGI camera effectiveness. Reassessing the previous studies' accuracy with this algorithm should be pursued. Secondly, the applied experimental data set acted as a proof of concept, therefore further experimentation should be completed with the a larger dataset to increase confidence in results.

As this method has the current application of analyzing experimentation in a controlled environment, further streamlining the export process has the potential to provide researchers with instantaneous feedback of the plume coverage fraction and further the likelihood of human detection. In closing, an accurate computational method to remove error associated with camera operator's judgment to apply to controlled research experimentation is a crucial objective that motivated this work and should be seen to fruition.

# Bibliography

[1] U.S. Enviromental Protection Agency. U.s. utility-scale electricity generation by source. Technical report, U.S. Enviromental Protection Agency, 2018.

[2] U.S. Energy Information Administration. Energy explained. Technical report, U.S. Energy Information Administration, 2020.

[3] Zheng Qiao, Qinglai Guo, Hongbin Sun, Zhaoguang Pan, Yuquan Liu, and Wen Xiong. An interval gas flow analysis in natural gas and electricity coupled networks considering the uncertainty of wind power. *Applied Energy*, 201:343–353, sep 2017.

[4] Meysam Qadrdan, Modassar Chaudry, Nick Jenkins, Pranab Baruah, and Nick Eyre. Impact of transition to a low carbon power system on the GB gas network. *Applied Energy*, 151:1–12, aug 2015.

[5] Modassar Chaudry, Nick Jenkins, Meysam Qadrdan, and Jianzhong Wu. Combined gas and electricity network expansion planning. *Applied Energy*, 113:1171–1187, jan 2014.

[6] Nai-Yuan Chiang and Victor M. Zavala. Large-scale optimal control of interconnected natural gas and electrical transmission systems. *Applied Energy*, 168:226–235, apr 2016.

[7] Luigi Mongibello, Nicola Bianco, Martina Caliano, and Giorgio Graditi. Comparison between two different operation strategies for a heat-driven residential natural gas-fired CHP system: Heat dumping vs. load partialization. *Applied Energy*, 184:55–67, dec 2016.

[8] Alessandro Spoladore, Davide Borelli, Francesco Devia, Flavio Mora, and Corrado Schenone. Model for forecasting residential heat demand based on natural gas consumption and energy performance indicators. *Applied Energy*, 182:488–499, nov 2016.

[9] Union Gas. Natural gas chemical composition. Technical report, Union Gas, 2019.

[10] Direct Global Warming Potentials. Direct global warming potentials. Technical report, Direct Global Warming Potentials, 2020.

[11] R. K. Pachauri, M. Allen, V. Barros, J. Broome, W. Cramer, R. Christ, J. Church, L. Clarke, Q. Dahe, and P. et al. Dasgupta. Contribution of working groups i, iiand iii to the fifth assessment report of the intergovernmental panelon climate change. Technical report, ClimateChange 2014: Synthesis Report, 2014.

[12] David R. Lyon, Ramón A. Alvarez, Daniel Zavala-Araiza, Adam R. Brandt, Robert B. Jackson, and Steven P. Hamburg. Aerial surveys of elevated hydrocarbon emissions from oil and gas production sites. *Environmental Science & Technology*, 50(9):4877–4886, apr 2016.

[13] Adam Brandt. Methane leaks from northamerican natural gas systems. *Science*, 2014.

[14] Anna Karion, Colm Sweeney, Eric A. Kort, Paul B. Shepson, Alan Brewer, Maria Cambaliza, Stephen A. Conley, Ken Davis, Aijun Deng, Mike Hardesty, Scott C. Herndon, Thomas Lauvaux, Tegan Lavoie, David Lyon, Tim Newberger, Gabrielle Pétron, Chris Rella, Mackenzie Smith, Sonja Wolter, Tara I. Yacovitch, and Pieter Tans. Aircraft-based estimate of total methane emissions from the barnett shale region. *Environmental Science & Technology*, 49(13):8124–8131, jul 2015.

[15] Tegan N. Lavoie, Paul B. Shepson, Maria O. L. Cambaliza, Brian H. Stirm, Anna Karion, Colm Sweeney, Tara I. Yacovitch, Scott C. Herndon, Xin Lan, and David Lyon. Aircraft-based measurements of point source methane emissions in the barnett shale basin. *Environmental Science & Technology*, 49(13):7904–7913, jul 2015.

[16] David R. Lyon, Daniel Zavala-Araiza, Ramón A. Alvarez, Robert Harriss, Virginia Palacios, Xin Lan, Robert Talbot, Tegan Lavoie, Paul Shepson, Tara I. Yacovitch, Scott C. Herndon, Anthony J. Marchese, Daniel Zimmerle, Allen L. Robinson, and Steven P. Hamburg. Constructing a spatially resolved methane emission inventory for the barnett shale region. *Environmental Science & Technology*, 49(13):8147–8157, jul 2015.

[17] Xin Lan, Robert Talbot, Patrick Laine, and Azucena Torres. Characterizing fugitive methane emissions in the barnett shale area using a mobile laboratory. *Environmental Science & Technology*, 49(13):8139–8146, jul 2015.

[18] Kathryn McKain, Adrian Down, Steve M. Raciti, John Budney, Lucy R. Hutyra, Cody Floerchinger, Scott C. Herndon, Thomas Nehrkorn, Mark S. Zahniser, Robert B. Jackson, Nathan Phillips, and Steven C. Wofsy. Methane emissions from natural gas infrastructure and use in the urban region of boston, massachusetts. *Proceedings of the National Academy of Sciences*, 112(7):1941–1946, jan 2015.

[19] et al Brandt, A. R. Methane leaks from north american natural gas systems. *Science*, 343(6172):733–735, 2014.

[20] et al. Alvarez, R. A. Greater focus needed on methane leakage from natural gas infrastructure. *Proceedings of the National Academy of Sciences*, 109(17):6435–6440, 2012.

[21] Katsumasa Tanaka, Otávio Cavalett, William J. Collins, and Francesco Cherubini. Asserting the climate benefits of the coal-to-gas shift across temporal and spatial scales. *Nature Climate Change*, 9(5):389–396, apr 2019.

[22] Yue Qin, Ryan Edwards, Fan Tong, and Denise L. Mauzerall. Can switching from coal to shale gas bring net carbon reductions to china? *Environmental Science & Technology*, 51(5):2554–2562, feb 2017.

[23] Roger Lueken, Kelly Klima, W. Michael Griffin, and Jay Apt. The climate and health effects of a USA switch from coal to gas electricity generation. *Energy*, 109:1160–1166, aug 2016.

[24] United States Environmental Protection Agency. New source performance standards. Technical report, United States Environmental Protection Agency, 2020.

[25] Candian Government. Sor/2018-66 - table of contents sor/2018-66regulations respecting reduction in the release of methane and certain volatile organic compounds (upstream oil and gas sector) (sor/2018-66). Technical report, Canada's System of Justice, 2020.

[26] Oil & gas operating and maintenance plans. Oil & gas operating and maintenance plans. Technical report, Colorado Deptartment of Public Health and Enviroment, 2018.

[27] California Air Resources Board. Oil and gas methane regulation. Technical report, California Air Resources Board, 2017.

[28] Environment and Climate Change Canada. National inventory report 1990–2014: Greenhousegas sources and sinks in canada part 1. Technical report, Environment and Climate Change Canada, 2015.

[29] Derek J. Reese and Duane R. McGregor. Optical gas imaging leak/no-leak emissions factor development using site-specific method 21 leak detection and repair data. In *Air Quality Measurement Methods and Technology*, 2019.

[30] FLIR Systems. Flir g400a manual. Technical report, FLIR Systems Inc., Wilsonville, OR, 2011, 2020.

[31] Arvind P. Ravikumar, Jingfan Wang, and Adam R. Brandt. Are optical gas imaging technologies effective for methane leak detection? *Environmental Science & Technology*, 51(1):718–724, dec 2016.

[32] W.M. Grundy, S.J. Morrison, M.J. Bovyn, S.C. Tegler, and D.M. Cornelison. Remote sensing d/h ratios in methane ice: Temperature-dependent absorption coefficients of ch3d in methane ice and in nitrogen ice. *Icarus*, 212(2):941–949, apr 2011.

[33] Jingfan Wang, Lyne P. Tchapmi, Arvind P. Ravikumar, Mike McGuire, Clay S. Bell, Daniel Zimmerle, Silvio Savarese, and Adam R. Brandt. Machine vision for natural gas methane emissions detection using an infrared camera. *Applied Energy*, 257:113998, jan 2020.

[34] Arvind P Ravikumar and Adam R Brandt. Designing better methane mitigation policies: the challenge of distributed small sources in the natural gas sector. *Environmental Research Letters*, 12(4):044023, apr 2017.

[35] T Footer. *Optical Gas Imaging Protocol*. Eastern Research Group, Inc. for U.S. Environmental Protection Agency, 2015.

[36] Arvind P. Ravikumar, Jingfan Wang, Mike McGuire, Clay S. Bell, Daniel Zimmerle, and Adam R. Brandt. "good versus good enough?" empirical tests of methane leak detection sensitivity of a commercial infrared camera. *Environmental Science & Technology*, 52(4):2368–2374, jan 2018.

[37] FLIR Systems. *FLIRGFx320 Infrared Camera for Methane, Hydrocarbon, and VOC Detection*.

[38] Yen-Chia Hsu, Paul Dille, Randy Sargent, and Illah R. Nourbakhsh. Industrial smoke detection and visualization. *CoRR*, abs/1809.06263, 2018.

[39] Turgay Celik, Huseyin Ozkaramanli, and Hasan Demirel. Fire and smoke detection without sensors: Image processing based approach. *IEEE*, 2007.

[40] C.-Y Lee, C.-T Lin, C.-T Hong, and M.-T Su. Smoke detection using spatial and temporal analyses. *International Journal of Innovative Computing, Information and Control*, 8:4749–4770, 07 2012.

[41] R.J. Radke, S. Andra, O. Al-Kofahi, and B. Roysam. Image change detection algorithms: a systematic survey. *IEEE Transactions on Image Processing*, 14(3):294–307, mar 2005.

[42] Simone Calderara, Paolo Piccinini, and Rita Cucchiara. Smoke detection in video surveillance: A MoG model in the wavelet domain. In *Lecture Notes in Computer Science*, pages 119–128. Springer Berlin Heidelberg, 2015.

[43] Jayavardhana Gubbi, Slaven Marusic, and Marimuthu Palaniswami. Smoke detection in video using wavelets and support vector machines. *Fire Safety Journal*, 44(8):1110–1115, nov 2009.

[44] Ke Gu, Zhifang Xia, Junfei Qiao, and Weisi Lin. Deep dual-channel neural network for image-based smoke detection. *IEEE Transactions on Multimedia*, 22(2):311–323, feb 2020.

[45] Simon Philipp Hohberg. Wildfire smoke detection usingconvolutional neural networks. Master's thesis, Freie Universität Berlin, 2015.

[46] Sebastien Frizzi, Rabeb Kaabi, Moez Bouchouicha, Jean-Marc Ginoux, Eric Moreau, and Farhat Fnaiech. Convolutional neural network for video fire and smoke detection. In *IECON 2016 - 42nd Annual Conference of the IEEE Industrial Electronics Society*. IEEE, oct 2016.

[47] Maria Araujo. Automated methane fugitiveemissions detection usingartificial intelligence andoptical gas imagers. In *Southwest Research Institute*, 2019.

[48] H.M. Abdel-Moati, J.M. Morris, Y. Ruan, and Y. Zeng. Remote gas detection system using infrared camera technology and sophisticated gas plume detection computer algorithm. In *SPE Annual Technical Conference and Exhibition*. Society of Petroleum Engineers, 2013.

[49] Rebellion Photonics. Gas cloud imaging system. Technical report, Rebellion Photonics, Janurary 2020.

[50] FLIR. Flir partners with providence photonics for gas leak quantification. Technical report, FLIR Systems, Inc, December 1, 2017.

[51] Yousheng Zeng and Jon Morris. Detection limits of optical gas imagers as a function of temperature differential and distance. *Journal of the Air & Waste Management Association*, 69(3):351–361, nov 2018.

[52] Yousheng Zeng, Jon Morris, Albert Sanders, Srikanth Mutyala, and Cory Zeng. Methods to determine response factors for infrared gas imagers used as quantitative measurement devices. *Journal of the Air & Waste Management Association*, 67(11):1180–1191, oct 2016.

[53] Austin L. Mitchell, Daniel S. Tkacik, Joseph R. Roscioli, Scott C. Herndon, Tara I. Yacovitch, David M. Martinez, Timothy L. Vaughn, Laurie L. Williams, Melissa R. Sullivan,

Cody Floerchinger, Mark Omara, R. Subramanian, Daniel Zimmerle, Anthony J. Marchese, and Allen L. Robinson. Measurements of methane emissions from natural gas gathering facilities and processing plants: Measurement results. *Environmental Science & Technology*, 49(5):3219–3227, feb 2015.

[54] Adam P. Pacsi, Tom Ferrara, Kailin Schwan, Paul Tupper, Miriam Lev-On, Reid Smith, and Karin Ritter. Equipment leak detection and quantification at 67 oil and gas sites in the western united states. *Elem Sci Anth*, 7(1):29, jul 2019.

[55] Enviromental Protection Agency. Method 21 - volatile organic compound leaks. Technical report, Enviromental Protection Agency, 2020.

[56] L. Rothman, I. Gordon, Y. Babikov, A. Barbe, D. C. Benner, P. Bernath, M. Birk, L. Bizzocchi, V. Boudon, L. Brown, and et al. The hitran2012 molecular spectroscopic database. *Journal of Quantitative Spectroscopy & Radiative Transfer*, 130(4-50):4–50, nov 2013.

[57] Craig O'Neill. Understanding cooled vs uncooled optical gas imaging. In *Air Quality Measurement Methods and Technology*, 2019.

[58] Theodore Bergman. *Fundamentals of Heat and Mass Transfer*. Don Fowley, Somerset, 2011.

[59] FLIR Systems Inc. The science behind optical gas imaging. Technical report, FLIR Systems Inc., 2020.

[60] Energy Institute Colorado State University. Methane emissions and technology evaluation center. Technical report, Colorado State University, Energy Institute, 2020.

[61] Omega Engineering. T type air process heaters for in-line air and gas heating. Technical report, Omega Engineering, 2020.

[62] Omega Engineering. 1/32 din autotune temperature/process dual setpoint controllers. Technical report, Omega Engineering, 2020.

[63] Thermocouple Info. Type k thermocouple. Technical report, Thermocouple Info, 2020.

[64] Francisco-Javier Mesas-Carrascosa, Fernando Pérez-Porras, Jose Meroño de Larriva, Carlos Mena Frau, Francisco Aguera-Vega, Fernando Carvajal-Ramírez, Patricio Martínez-Carricondo, and Alfonso García-Ferrer. Drift correction of lightweight microbolometer thermal sensors on-board unmanned aerial vehicles. *Remote Sensing*, 10(4):615, apr 2018.

[65] Robert Olbrycht and Bogusław Więcek. New approach to thermal drift correction in microbolometer thermal cameras. *Quantitative InfraRed Thermography Journal*, 12(2):184–195, jul 2015.

[66] Olivier Riou, Stephane Berrebi, and Pierre Bremond. Nonuniformity correction and thermal drift compensation of thermal infrared camera. In Douglas D. Burleigh, K. Elliott Cramer, and G. Raymond Peacock, editors, *Thermosense XXVI*. SPIE, apr 2004.

[67] EdmundLai PhD. Converting analog to digital signals and vice versa. *Practical Digital Signal Processing*, pages 14–49, 2003.

[68] MATLAB. 1-d digital filter. Technical report, MATLAB Signal Processing Toolbox, March 2, 2020.

[69] MATLAB. 2-d gaussian filtering of images. Technical report, MATLAB Signal Processing Toolbox, March 2, 2020.

# Appendix A

# Developed Software Packages

The following developed software packages are uploaded and available in a GitHub repository:

*HexImager Software Package*

These are located at https://github.com/marcus858/OGI-Frequency-Based-Algorithm